



**HAL**  
open science

## Ge(Sn) growth on Si(001) by magnetron sputtering

H. Khelidj, A. Portavoce, M. Bertoglio, M. Descoins, L. Patout, K. Hoummada, A. Hallén, A. Charai, M.C. Benoudia, D. Mangelinck

### ► To cite this version:

H. Khelidj, A. Portavoce, M. Bertoglio, M. Descoins, L. Patout, et al.. Ge(Sn) growth on Si(001) by magnetron sputtering. *Materials Today Communications*, 2020, pp.101915. 10.1016/j.mtcomm.2020.101915 . hal-03065804

**HAL Id: hal-03065804**

**<https://hal.science/hal-03065804v1>**

Submitted on 15 Dec 2020

**HAL** is a multi-disciplinary open access archive for the deposit and dissemination of scientific research documents, whether they are published or not. The documents may come from teaching and research institutions in France or abroad, or from public or private research centers.

L'archive ouverte pluridisciplinaire **HAL**, est destinée au dépôt et à la diffusion de documents scientifiques de niveau recherche, publiés ou non, émanant des établissements d'enseignement et de recherche français ou étrangers, des laboratoires publics ou privés.

# Ge(Sn) growth on Si(001) by magnetron sputtering

H. Khelidj<sup>1,2</sup>, A. Portavoce<sup>1,\*</sup>, M. Bertoglio<sup>1</sup>, M. Descoins<sup>1</sup>, L. Patout<sup>1</sup>, K. Hoummada<sup>1</sup>, A. Hallén<sup>3</sup>, A. Charai<sup>1</sup>, M. C. Benoudia<sup>2</sup>, and D. Mangelinck<sup>1</sup>

<sup>1</sup>IM2NP, CNRS/Aix-Marseille University, Faculté des Sciences de Saint-Jérôme case 142, 13397 Marseille, France

<sup>2</sup>Ecole Nationale Supérieure des Mines et de la Métallurgie, L3M, Annaba, Algeria

<sup>3</sup>KTH, Royal Institute of Technology, School of Electrical Engineering and Computer Science (EECS), SE-164 40 Kista-Stockholm, Sweden

## ABSTRACT

The semi-conductor  $\text{Ge}_{1-x}\text{Sn}_x$  exhibits interesting properties for optoelectronic applications. In particular,  $\text{Ge}_{1-x}\text{Sn}_x$  alloys with  $x \geq 0.1$  exhibit a direct band-gap, and integrated in complementary-metal-oxide-semiconductor (CMOS) technology, should allow the development of Si photonics. CMOS-compatible magnetron sputtering deposition was shown to produce monocrystalline  $\text{Ge}_{1-x}\text{Sn}_x$  films with good electrical properties at low cost. However, these layers were grown at low temperature ( $< 430$  K) and contained less than 6% of Sn. In this work,  $\text{Ge}_{1-x}\text{Sn}_x$  thin films were elaborated at higher temperature ( $> 600$  K) on Si(001) by magnetron sputtering in order to produce low-cost and CMOS-compatible relaxed pseudo-coherent layers with  $x \geq 0.1$  exhibiting a better crystallinity.  $\text{Ge}_{1-x}\text{Sn}_x$  crystallization and  $\text{Ge}_{1-x}\text{Sn}_x$  crystal growth were investigated. Crystallization of an amorphous  $\text{Ge}_{1-x}\text{Sn}_x$  layer deposited on Si(001) or Ge(001) grown on Si(001) leads to the growth of polycrystalline films. Furthermore, the competition between Ge/Sn phase separation and  $\text{Ge}_{1-x}\text{Sn}_x$  growth prevents the formation of large-grain Sn-rich  $\text{Ge}_{1-x}\text{Sn}_x$  layers without the formation of  $\beta$ -Sn islands on the layer surface, due to significant atomic redistribution kinetics at the crystallization temperature ( $T = 733$  K for  $x = 0.17$ ). However, the growth at  $T = 633$  K of a highly-relaxed pseudo-coherent  $\text{Ge}_{0.9}\text{Sn}_{0.1}$  film with low impurity concentrations ( $< 2 \times 10^{19}$  at  $\text{cm}^{-3}$ ) and an electrical resistivity four orders of

magnitude smaller than undoped Ge is demonstrated. Consequently, magnetron sputtering appears as an interesting technique for the integration of optoelectronic and photonic devices based on  $\text{Ge}_{1-x}\text{Sn}_x$  layers in the CMOS technology.

*Keywords:* GeSn, Magnetron Sputtering, Silicon substrate, Epitaxy

\*Corresponding author: [alain.portavoce@im2np.fr](mailto:alain.portavoce@im2np.fr)

## 1. Introduction

Current microelectronic device production is based on the complementary-metal-oxide-semiconductor (CMOS) technology [1-2]. This technology has significantly evolved over the years due to device size reduction requirements and partly relies on thin film deposition, growth, and patterning capabilities at the nanometer scale [3]. It is currently based on Silicon (Si) and Germanium (Ge) semiconductors and their alloys, as well as on the use of different metals (Cu, Ni, Pt...), oxides (SiO<sub>2</sub>, HfO<sub>2</sub>...) and nitrides (Si<sub>3</sub>N<sub>4</sub>, TiN...) [4-8]. This technology provides a high production rate of cost-effective integrated nanostructured devices with high levels of purity and reliability. Photonics is a well-established technology allowing for high speed communication [9-10]. However, the integration of photonic devices and circuits in microelectronic chips would promote the development of new optoelectronic technologies, boosting the capacity of current electronic devices [11-14]. Standard CMOS technology already allows the integration of photonic devices such as waveguides (Si nitrides), SiGe-based optical modulators, and Ge- or SiGe-based photodetectors [15-19]. However, Si and Ge being indirect band-gap semiconductors, an essential photonic element is missing for full integrated CMOS Si-photonic development: a light source (i.e. laser integration). Ge<sub>1-x</sub>Sn<sub>x</sub> is a CMOS-compatible IV-IV semiconductor exhibiting interesting properties for infrared photodetector, light emitting diode, and laser fabrication [20-26]. Furthermore, Ge<sub>1-x</sub>Sn<sub>x</sub> alloys can be used for the fabrication of integrated optical amplifier, Gas sensors [27], and high-speed thin-film transistors [28-29], and direct band-gap Ge<sub>1-x</sub>Sn<sub>x</sub> alloys are of high interest for solar cells [30]. Ge<sub>1-x</sub>Sn<sub>x</sub> single crystals are expected to be best suited for all these applications, since grain boundaries (GB) in polycrystalline films create deep band-gap levels and act as effective recombination centers, and impair device efficiency. For example, the electronic behavior of polycrystalline semiconductors

is strongly dependent on grain size. GB scattering decreases charge carrier mobility, which can increase linearly with grain size at constant temperature [28]. In the case of *p*-doped Ge, an inversion from *p*-type to *n*-type can be observed if the trap energy level in GB lies in the upper half of the band-gap [31].

The  $\text{Ge}_{1-x}\text{Sn}_x$  alloy is expected to exhibit a direct band-gap for Sn compositions of 10 at% ( $x = 0.1$ ) and above, as required for laser fabrication [32-34]. However, the maximum Sn solubility limit in Ge is  $\sim 1.1$  at % at 673 K [35-36]. Consequently, only metastable Sn-rich  $\text{Ge}_{1-x}\text{Sn}_x$  layers can be produced [37]. The microcrystalline, optical and electrical properties of  $\text{Ge}_{1-x}\text{Sn}_x$  films may consequently be highly dependent on fabrication techniques and conditions. Furthermore, the large difference of lattice parameters between Si and  $\text{Ge}_{1-x}\text{Sn}_x$  alloys increases growth complexity, the lattice parameter of diamond Sn being 19.5% larger than the Si lattice parameter [38]. Semiconductor growth is usually performed using chemical vapor deposition (CVD) [39] or molecular beam epitaxy (MBE) [40], to produce defect-free and contamination-free layers, compatible with microelectronic technology requirements. The sputtering technique is CMOS-compatible and significantly low-cost compared to the CVD and MBE techniques [41]. However, sputtered layers are expected to be highly contaminated, in particular with O and C, and to exhibit poor electrical properties compared to layers grown by MBE or CVD.  $\text{Si}_{1-x}\text{Ge}_x$  layers are currently grown by CVD in the CMOS technology [42-43], while magnetron sputtering is used for ohmic contact fabrication for example [44-45]. However, high quality  $\text{Ge}_{1-x}\text{Sn}_x$  material can be obtained by sputtering:  $\text{Ge}_{1-x}\text{Sn}_x$ -based photodetectors using a  $\text{Ge}_{0.94}\text{Sn}_{0.06}$  active layer grown by sputtering were shown to exhibit a dark-current density and a responsivity comparable with similar devices using MBE-grown  $\text{Ge}_{1-x}\text{Sn}_x$  layers [46]. The growth of  $\text{Ge}_{1-x}\text{Sn}_x$  thin films by sputtering have been investigated less often than using CVD or MBE.  $\text{Ge}_{1-x}\text{Sn}_x$

layers directly sputtered on an Si(001) substrate are usually polycrystalline [47-49], but monocrystalline sputtered  $\text{Ge}_{1-x}\text{Sn}_x$  layers can be grown on Ge(001) and GaAs(001) substrates, using low growth temperatures between 423 and 443 K [50-51]. Zheng et al. [52] succeeded to grow  $\text{Ge}_{1-x}\text{Sn}_x$  single crystals on Si(001) substrates using the growth of a sputtered Ge buffer on the Si substrate before  $\text{Ge}_{1-x}\text{Sn}_x$  deposition. The Ge buffer was grown at  $T = 673$  K, but the  $\text{Ge}_{1-x}\text{Sn}_x$  film was grown at  $T = 423$  K with  $x \leq 0.06$ .  $\text{Ge}_{1-x}\text{Sn}_x$  films grown or annealed at higher temperatures generally exhibit better crystal quality and thus better electrical properties [53]. Low temperature growth is necessary to ensure Sn incorporation. CVD or MBE growths of  $\text{Ge}_{1-x}\text{Sn}_x$  are usually performed at temperatures comprised between 473 and 723 K, and the obtained films are sometimes annealed at higher temperatures in order to improve the electrical and optical properties [54-55].

The indirect-to-direct band gap transition occurring at lower Sn composition for relaxed  $\text{Ge}_{1-x}\text{Sn}_x$  films [56-58], the present work aims to investigate the low-cost high-temperature growth of relaxed monocrystalline  $\text{Ge}_{1-x}\text{Sn}_x$  films on Si(001) with  $x \geq 0.1$  in a commercial magnetron sputtering setup. Indeed, relaxed  $\text{Ge}_{0.9}\text{Sn}_{0.1}$  films were grown at  $T = 633$  K in pseudo-epitaxy on Si(001) using magnetron sputtering. These films contain impurity concentrations lower than  $2 \times 10^{19}$  at  $\text{cm}^{-3}$  and exhibit an electrical resistivity four orders of magnitude lower than that of undoped Ge.

## 2. Experiments

Ge and Sn were co-deposited on Si(001) substrates using a 99.9999% pure Ar gas flow to simultaneously sputter in DC mode a 99.999% pure Ge target and a 99.99% pure Sn target, in a commercial magnetron sputtering system exhibiting a base pressure of  $10^{-8}$  Torr. In this setup,

the sample is mounted on a horizontal rotating sample holder, and three targets can be placed symmetrically ( $120^\circ$  angle between each target) above the sample, with an angle of  $45^\circ$  between the normals of the target surfaces and the sample surface. Deposition was performed at the pressure of  $2.25 \times 10^{-3}$  Torr. The sample was rotating at a speed of 5 rpm and was set to ground level, while a voltage was applied to each target to maintain a constant power during deposition. The Ge target was sputtered at the power of 15 W during the deposition of the Ge buffer, corresponding to a deposition rate of  $0.09 \text{ nm s}^{-1}$ .  $\text{Ge}_{1-x}\text{Sn}_x$  was deposited during 96 s with a power of 150 W for the Ge target and a power of 15 W for the Sn target, corresponding to a deposition rate of  $0.84 \text{ nm s}^{-1}$  for Ge and of  $0.21 \text{ nm s}^{-1}$  for Sn. The Ge and Sn fluxes were calibrated separately, using X-ray reflectivity to determine the thicknesses of sputtered films deposited at room temperature (RT) in different conditions. In the following, the nominal composition of the films, i.e. calculated from the Ge and Sn fluxes taking into account the atomic volume difference between Ge and Sn ( $\Omega_{\text{Sn}}/\Omega_{\text{Ge}} \sim 1.2$ ), will be given unless otherwise specified. The Si substrates were dipped in a 5% HF solution in order to remove the Si native oxide before being loaded in the growth chamber. The structure of the  $\text{Ge}_{1-x}\text{Sn}_x$  films was studied by X-ray diffraction (XRD) in the Bragg-Brentano geometry ( $\theta$ - $\theta$ ) using a Cu  $\text{K}\alpha$  source ( $\lambda_{\text{K}\alpha} = 0.154 \text{ nm}$ ) in a PANalytical X'Pert PRO setup equipped with an X'Celerator detector designed for high speed data collection. This setup was also used to perform *in situ* XRD measurements during amorphous  $\text{Ge}_{1-x}\text{Sn}_x$  film crystallization. In this case, the temperature was raised from 423 to 853 K following a heating ramp made of 5 K per minute steps separated by 5 min long XRD measurements at constant temperature, corresponding to an average heating ramp of  $1 \text{ K min}^{-1}$ . Structural observations were also performed using transmission electron microscopy (TEM). Scanning TEM Dark-Field (STEM-DF) and Energy Dispersive X-Ray Spectrometry (EDS)

analyses were acquired at 200 keV using a LaB<sub>6</sub> Thermo Fisher Tecnai TEM equipped with a silicon drift detector OXFORD X-max80. High-Resolution TEM images were performed at 200 keV using a field emission gun Thermo Fisher Titan microscope equipped with a spherical aberration (Cs) correction system. We consider the Cs value in an order of magnitude between 0 and -0.05 mm allowing a point-to-point resolution around 1 Å to be reached. The surface topography of the layers was studied using scanning electron microscopy (SEM) and atomic force microscopy (AFM). AFM images were obtained in non-contact mode using a PSIA XE-100 in air microscope. The composition of the layers was determined using Rutherford backscattering (RBS) and atom probe tomography (APT). For the RBS, 2.0 MeV alpha particles were used with a backscatter detector positioned at 170°. SEM images as well as the TEM and APT sample preparations were performed in an FEI dual beam HELIOS 600 nanolab setup. APT measurements were performed at  $T = 50$  K using a laser-pulsed CAMECA LEAP 3000XHR microscope, with a laser pulse frequency of 100 kHz and a laser power of 0.2 nJ. The resistivity of the films was measured at RT by the four probe method.

### 3. Results and discussion

#### 3.1. Ge(Sn) Crystallization

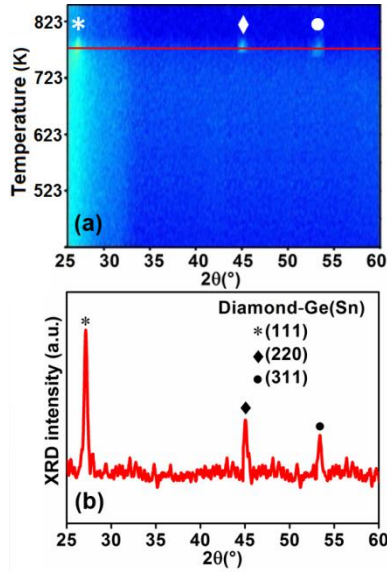


**FIG. 1.** a) XRD measurements performed during the *in situ* annealing of an amorphous  $\text{Ge}_{0.83}\text{Sn}_{0.17}$  film deposited on Si(001), following an average ramp of  $\sim 1 \text{ K min}^{-1}$  from 423 to  $T = 853 \text{ K}$ ; and b) diffractogram acquired at  $T = 778 \text{ K}$  during the *in situ* annealing (red line in a).

**Fig. 1a** presents *in situ* XRD measurements recorded during annealing a 100 nm-thick  $\text{Ge}_{0.83}\text{Sn}_{0.17}$  film deposited at room temperature on Si(001). No diffraction peaks are observed after deposition, the film being amorphous. Three diffraction peaks at  $2\theta = 26.92^\circ$ ,  $44.70^\circ$ , and  $52.87^\circ$  appear simultaneously during the annealing ramp, when the temperature reaches  $T = 733 \text{ K}$ . They respectively correspond to the atomic planes (111), (220), and (311) of the  $\text{Ge}_{1-x}\text{Sn}_x$  diamond structure (**fig. 1b**). Surprisingly, one can note that their intensity decreases when the temperature increases, and the peaks disappear concurrently, leaving no diffraction signal at  $T = 853 \text{ K}$ .

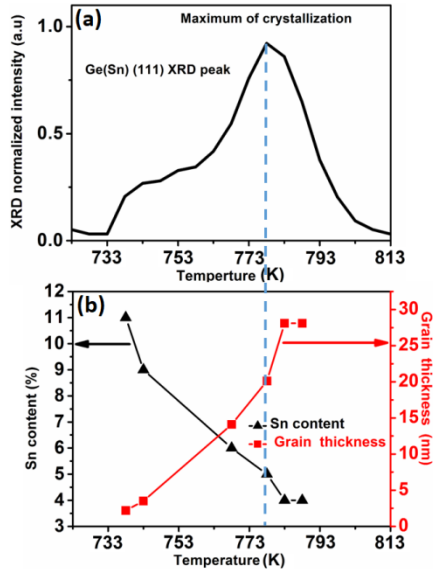


**FIG. 2.** XRD measurements performed during the *in situ* annealing of an amorphous  $\text{Ge}_{0.83}\text{Sn}_{0.17}$  film deposited on Si(001), following an average ramp of  $\sim 1 \text{ K min}^{-1}$  from 523 to  $T = 853 \text{ K}$ : a) integrated and normalized intensity of the  $\text{Ge}_{1-x}\text{Sn}_x(111)$  diffraction peak versus temperature, and b) average grain size determined from the half-maximum width of the (111) peak using the Scherrer equation (solid squares, right axis), and Sn concentration determined from the diffraction angle  $2\theta$  of the (111) peak (solid triangles, left axis).

Fig. 2a shows the intensity variation of the (111) peak recorded during the annealing ramp. The peak is detected at  $T = 733 \text{ K}$  and its intensity increases with temperature up to  $T = 778 \text{ K}$ . This stage corresponds to the nucleation followed by the growth of the  $\text{Ge}_{1-x}\text{Sn}_x$  crystal from the initial amorphous film. For temperatures higher than  $T = 778 \text{ K}$ , the intensity of the (111) diffracted peak decreases and finally disappears at  $T = 818 \text{ K}$ , without the apparition of other diffraction peaks until the end of the annealing at  $T = 873 \text{ K}$ . In order to understand this behavior, the variations of the full width at half maximum (FWHM) of the (111) peak were analyzed using the Scherrer equation, giving the average grain size in the direction perpendicular to the film surface [59]. The “thickness” variations versus temperature of the  $\text{Ge}_{1-x}\text{Sn}_x$  grains with (111) planes oriented parallel to the film surface are shown in fig. 2b (solid squares, right axis). The data should be interpreted qualitatively since parameters other than grain size could also modify the FWHM of diffraction peaks. However, one can note that the grain size is significantly smaller than the film thickness. The grain size is less than 3 nm when the diffraction peak is first detected, and increases with temperature to reach a maximum size of about 30 nm at  $T = 783 \text{ K}$ ,

in agreement with the nucleation and growth of the  $\text{Ge}_{1-x}\text{Sn}_x$  polycrystalline film up to this temperature. The size of the  $\text{Ge}_{1-x}\text{Sn}_x$  grains stays constant after  $T = 783$  K, despite the decrease of the diffraction peak intensity (fig. 2a). The variations of the diffraction angle  $2\theta$  of the (111) peak were investigated considering the polycrystalline  $\text{Ge}_{1-x}\text{Sn}_x$  layer fully relaxed, and its lattice parameter  $a_{\text{GeSn}}$  following the corrected-Vegard law:

$$a_x^{\text{GeSn}} = (1 - x)a_{\text{Ge}} + xa_{\text{Sn}} + bx(1 - x) \quad (1)$$

$a_{\text{Ge}} = 0.565$  nm,  $a_{\text{Sn}} = 0.649$  nm, and  $b = 0.0041$  nm are respectively the Ge and Sn lattice parameters in the diamond structure, and the bowing coefficient [48-60]. The average Sn content of the crystallized  $\text{Ge}_{1-x}\text{Sn}_x$  layer was deduced from this equation, using the Bragg equation [61] and the experimental diffraction angle  $2\theta$  to determine  $a_{\text{GeSn}}$ . Fig. 2b presents the variation of the Sn concentration in the  $\text{Ge}_{1-x}\text{Sn}_x$  grains versus temperature. The Sn concentration is about 11% at the beginning of crystallization, and continuously decreases as temperature increases, reaching 4% before the disappearance of the diffraction peak.  $\text{Ge}_{1-x}\text{Sn}_x$  crystallization at 733 K allowed Sn incorporation above 10% to be obtained. However, atom mobility is fast enough to support Ge and Sn phase separation at this temperature and above. As expected, the *in situ* XRD measurements reveal a strong competition between Sn incorporation and  $\text{Ge}_{1-x}\text{Sn}_x$  crystallization. As soon as the nucleation process is completed, the crystal growth rate as well as the Ge/Sn separation rate increase with temperature. One can note that the grain size and their Sn composition stay almost constant while the diffraction peak intensity decreases. This phenomenon can be explained by a lateral shrinking of the 30 nm-thick  $\text{Ge}_{0.96}\text{Sn}_{0.04}$  grains. Since  $\text{Ge}_{1-x}\text{Sn}_x$  grains lose Sn, an Sn-rich alloy should grow. However, this Sn-rich phase shows no

diffraction peak, meaning that either its grains exhibit crystallographic orientations not compatible with the  $\theta$ - $\theta$  diffraction geometry, or the phase is actually amorphous or liquid.

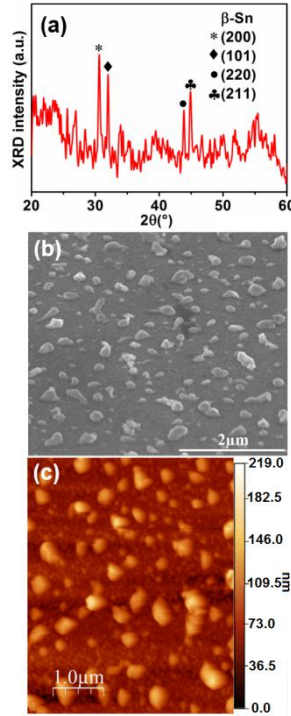


**FIG. 3.** Analyses performed at RT on the sample that experienced the XRD *in situ* annealing presented in Fig. 1 and 2: a) X-ray diffractogram, b) SEM measurements, and c) AFM measurements.

**Fig. 3a** shows the diffractogram measured on the sample at RT after the ramp annealing. Diffraction peaks corresponding to  $\beta$ -Sn are detected. Thus, the  $\text{Ge}_{1-x}\text{Sn}_x$  phase was probably consumed by the growth of liquid Sn, as the Sn bulk melting temperature is  $\sim 505$  K and can be lower for nanocrystals [62]. However, no diffraction peak corresponding to crystalline Ge is detected at RT, suggesting that the mechanism of Ge/Sn phase separation at high temperature in the thin film leads to the formation of amorphous Ge. **Fig. 3b** and **3c** present SEM and AFM images of the sample surface after annealing. Large islands are observed with a lateral size between 94 and 470 nm, an average height  $\sim 110$  nm, and a surface density  $\sim 8.4 \times 10^8 \text{ cm}^{-2}$ . The root-mean-square (RMS) surface roughness is  $\sim 26$  nm. These islands probably correspond to the Sn-rich phase that crystallized during sample cooling. **Fig. 4** presents STEM Dark-Field observations performed on the sample after the *in situ* XRD annealing. **Fig. 4a** shows a cross-

section view between two islands similar to that observed on the sample surface by SEM (Fig. 3b) and AFM (Fig. 3c). The Pt layer was deposited on the sample surface for TEM sample preparation. The islands are in direct contact with the Si substrate, as confirmed by High-Resolution TEM observations (Fig. 4b). One can note that the island/Si interface is flat and abrupt, which suggest that this interface corresponds to the initial Si substrate surface.

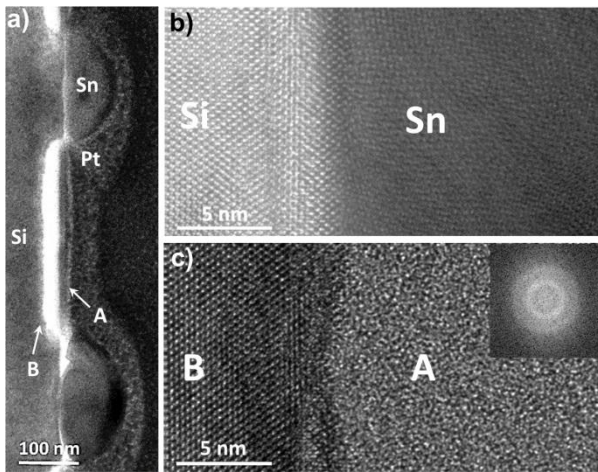


**FIG. 4.** Cross-section TEM measurements performed on the sample that experienced the XRD *in situ* annealing presented in Fig. 1 and 2: a) STEM Dark-Field image, b) and c) High-Resolution TEM images. The inset in c) presents the local FFT obtained on the layer A.

This is in agreement with the Si-Sn phase diagram [35], showing phase separation between Si and Sn. The maximum solubility of Sn in Si is 0.1 at% at 1339 K, while the solubility limit of Si in  $\beta$ -Sn is less than 0.5 at%. The stack of two layers (noted A and B in Fig. 4a) is observed between the two islands. Fig. 4c presents a High-Resolution TEM image of the interface between these two layers. The layer A is amorphous and its average thickness is  $\sim 25$  nm. As shown in the inset of Fig. 4c, a short-range order exists in the layer, corresponding to a distance of 0.32 nm (radius of the ring in the FFT pattern in the inset), which is significantly higher than the nearest neighbor distance ( $\sim 0.245$  nm) in the Ge crystal. Below this amorphous layer, a bright contrast is observed with an average thickness of  $\sim 30$  nm, corresponding to the layer B. Fig. 4c shows that this layer is crystalline and coherent with the Si crystal. EDS analyses (not shown) confirmed that

the islands contain only Sn atoms (in the detection limit of the technique). However, the overlapping of Ge and Pt signals prevented the Ge distribution in the sample to be determined. The TEM observations show that the mechanism of Ge/Sn phase separation is complex. Sn atoms are located in large islands exhibiting a height similar to the thickness of the amorphous  $\text{Ge}_{0.83}\text{Sn}_{0.17}$  layer initially deposited on Si (Fig. 4a). However, the Ge atoms seem to have been incorporated in the Si Substrate, part in an amorphous layer and part in the Si lattice, as the bright contrast of the layer B can be due to the presence in this region of atoms heavier than Si. Ge evaporation from the Si substrate and Ge lattice diffusion in Si cannot occur at 853 K. However, Sn migration in Ge is effective at this temperature, Sn atoms living the  $\text{Ge}_{1-x}\text{Sn}_x$  film to form liquid Sn droplets. Thus, Ge evaporation from the surface of melted Sn cannot be ruled out. According to Ge self-diffusion [63-64], Ge atom mobility is limited at 853 K (few nanometers after one hour), which can be the reason for the Ge layer to stay amorphous once emptied of the Sn atoms. The Ge/Si intermixing located in the layer B is difficult to explain considering equilibrium kinetic parameters such as lattice diffusion. This intermixing could occur only through short-circuit paths, such as interface diffusion/redistribution, or due to unusual high concentrations of point defects. XRD *in situ* isothermal annealing at  $T = 788$  K was performed on the same as-deposited  $\text{Ge}_{0.83}\text{Sn}_{0.17}$  film. The thermal annealing was stopped as soon as  $\text{Ge}_{1-x}\text{Sn}_x$  diffraction peaks were detected.

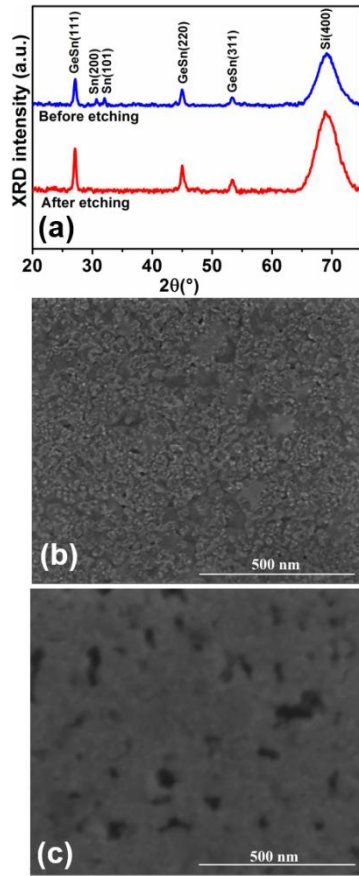


**FIG. 5.** Diffractograms measured at RT on an amorphous  $\text{Ge}_{0.83}\text{Sn}_{0.17}$  film deposited on the native silicon oxide formed on Si(001) and annealed at  $T = 788$  K for 6 min, before (top) and after (bottom) chemical etching in a 5% HF solution (a), and SEM images obtained on the same sample before (b) and after (c) chemical etching.

**Fig. 5a** shows the diffractogram (top) measured at RT on this sample after annealing. The diffraction peaks (111), (220), and (311) of the  $\text{Ge}_{1-x}\text{Sn}_x$  crystal are observed, as well as two diffraction peaks (not observed at  $T = 788$  K) at  $2\theta = 30.70^\circ$ , and  $32.06^\circ$ , corresponding to  $\beta$ -Sn(200) and  $\beta$ -Sn(101), respectively. These peaks are detected at the diffraction angle of pure  $\beta$ -Sn, indicating that the Ge content in the crystallized Sn islands should not be above the (relatively low) Ge solubility in Sn. The average Sn concentration in the  $\text{Ge}_{1-x}\text{Sn}_x$  grains is  $\sim 6\%$  and the average grain size is  $\sim 18$  nm from the XRD analysis. **Fig. 5b** presents an SEM image of the sample surface. A network of connected islands is observed. The sample was dipped in a 5% HF solution to remove the Sn-rich alloy located on the surface of the sample, before XRD measurements at RT (bottom diffractogram in **fig. 5a**) [65]. The diffraction peaks of the

$\text{Ge}_{0.94}\text{Sn}_{0.06}$  film are still detected after etching, but the diffraction peaks of  $\beta\text{-Sn}$  have disappeared. SEM images of the surface after etching (fig. 5c) show a flat surface with holes exhibiting lateral sizes between 19 and 160 nm, with a surface density  $\sim 2.7 \times 10^9 \text{ cm}^{-2}$ .

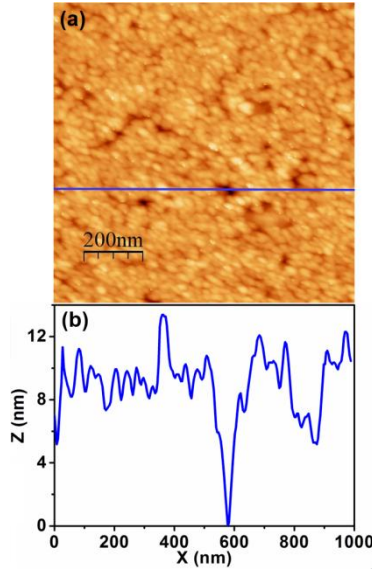


**FIG. 6.** AFM measurements performed on the same sample as in Fig. 5c, after annealing at  $T = 788 \text{ K}$  for 6 min and chemical etching in a 5% HF solution: a) surface topography, and b) 1D topography profile along the blue line shown in a).

AFM measurements (fig. 6) give an RMS surface roughness  $\sim 1.3 \text{ nm}$ , and an average lateral grain size  $\sim 25 \text{ nm}$ , which is in agreement with the  $\text{Ge}_{1-x}\text{Sn}_x$  grain size determined from the XRD peaks, considering the lateral inaccuracy involved with AFM in air due to tip effects. Obviously, these holes correspond to the locations of the  $\beta\text{-Sn}(\text{Ge})$  alloy and confirm that the Ge/Sn phase separation process should occur laterally in the layer, with the formation of a liquid  $\beta\text{-Sn}(\text{Ge})$  alloy, probably developing droplets on the  $\text{Ge}_{1-x}\text{Sn}_x$  surface.

These results show that the atomic mobility and the Ge/Sn phase separation kinetic are too high at the  $\text{Ge}_{1-x}\text{Sn}_x$  crystallization temperature to easily obtain large-grain Sn-rich polycrystalline  $\text{Ge}_{1-x}\text{Sn}_x$  layers without the formation of  $\beta\text{-Sn}$  from the crystallization process.

The limiting phenomenon is probably nucleation, since crystalline  $\text{Ge}_{1-x}\text{Sn}_x$  layers can be grown at lower temperatures.

### 3.2. Ge buffer growth

As reported in the literature,  $\text{Ge}_{1-x}\text{Sn}_x$  layers deposited on Si are usually polycrystalline. However, monocrystalline  $\text{Ge}_{1-x}\text{Sn}_x$  layers can be grown on Si substrate using the deposition of a Ge buffer on the Si substrate before the growth of the  $\text{Ge}_{1-x}\text{Sn}_x$  layer.

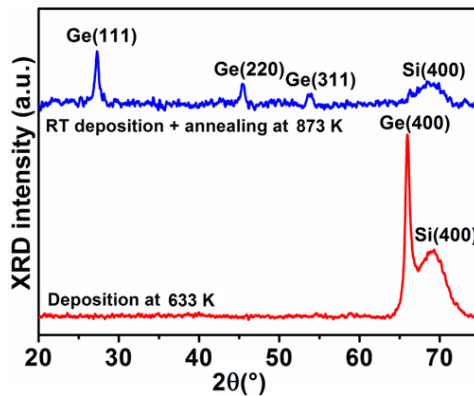


**FIG. 7.** X-ray diffractograms measured at RT on a 100 nm-thick Ge film deposited at RT on the Si(001) substrate and annealed at 873 K for 30 min (top) and a 100 nm-thick Ge film deposited on Si(001) at  $T = 633$  K (bottom).

**Fig. 7** presents the diffractogram measured at RT on a 100 nm-thick Ge layer deposited at RT on the Si(001) substrate and annealed at 873 K for 30 min under vacuum ( $P < 10^{-6}$  mbar). The Ge layer is polycrystalline as the (111), (220), and (311) diffraction peaks of the Ge diamond structure are detected at  $2\theta = 27.29^\circ$ ,  $45.54^\circ$ , and  $53.82^\circ$ , respectively. One can note that the polycrystalline Ge film exhibits the same peaks and the same peak intensity ratios as the polycrystalline  $\text{Ge}_{1-x}\text{Sn}_x$  films that are characteristics of a randomly oriented polycrystal with a diamond structure (Si, Ge,  $\text{Ge}_{1-x}\text{Sn}_x$ ...). **Indeed, thin film growth is highly dependent on surface and interface energies, and the surface and interface contributions in the overall film energy increases as the film thickness decreases. Depending on atom mobility during growth (growth**

conditions), the film tends to exhibit a texture allowing for energy minimization, as much as possible. The {111} and {113} surfaces are known to be low-energy surfaces of the diamond structure, while {110} facets are more easily observed on surfaces exhibiting low-level contamination of O and C. {111} and {113} facets are the equilibrium facets of relaxed Si and Ge crystals [66] and are observed on relaxed Si-Ge islands [67-68]. Consequently, if the surface contamination level stays low, the texture of polycrystalline Si, Ge and  $\text{Ge}_{1-x}\text{Sn}_x$  films generally shows a large fraction of grains exhibiting the {111} and {113} crystallographic orientations in the direction parallel to the film surface. The relaxed Ge lattice parameter  $a_{rel}$  is expected to be  $\sim 0.565$  nm at RT [69]. In the  $\theta$ - $\theta$  XRD geometry used in this study, the measured plane spacing corresponds to plane spacing in the direction perpendicular to the film surface and is thus denoted  $d_{\perp}^{exp}$ . The Ge film lattice parameter in the direction perpendicular to the surface  $a_{\perp}^{exp}$  was thus determined from the diffraction angles of the three diffraction peaks Ge(111), Ge(220), and Ge(311) using the Bragg equation. In average  $a_{\perp}^{exp} = 0.565$  nm, corresponding to a fully relaxed Ge polycrystalline layer. The Si lattice parameter was also determined from the Si(400) diffraction peak observed in the same diffractogram (fig. 7) for comparison. For the Si substrate  $a_{\perp}^{exp} = 0.543$  nm, as expected for relaxed Si [70].

The crystallization of a Ge layer deposited at RT on the Si(001) substrate cannot be used for growing a monocrystalline  $\text{Ge}_{1-x}\text{Sn}_x$  film, since it leads to the formation of a polycrystalline Ge buffer. Instead, the Ge buffer should be grown at a sufficiently high temperature to allow the Ge crystal to form in partial coherence with the Si substrate due to a high enough atomic mobility, but sufficiently low to prevent extensive Si/Ge intermixing and interdiffusion. Note that the epitaxy is only partially coherent because of the large thickness of the Ge layer and the large misfit between Si and Ge that lead to the nucleation of misfit dislocations. Fig. 7 shows XRD

measurements (bottom diffractogram) performed at RT on a 100 nm-thick Ge layer deposited by magnetron sputtering on Si(001) at  $T = 633$  K. This diffractogram corresponds to a Ge layer that is pseudo-coherent with the Si substrate: a single Ge diffraction peak is now observed at  $2\theta = 65.98^\circ$ , corresponding to the same orientation as the substrate Si(400) diffraction peak. RBS measurements (not shown) confirmed that the layer contains only Ge and that its thickness is  $\sim 100$  nm. XRD measurements give  $a_{\perp}^{exp} = 0.566$  nm, which indicates that the Ge layer is compressively strained on the Si substrate [71]. Considering that  $a_{rel} = 0.565$  nm for Ge, the perpendicular distortion  $\varepsilon_{\perp}^{exp}$  of this pseudo-coherent Ge layer was found to be  $\varepsilon_{\perp}^{exp} = 0.0018$ , using eq. 2 [72].

$$\varepsilon_{\perp,\parallel} = \frac{a_{\perp,\parallel} - a_{rel}}{a_{rel}} \quad (2)$$

Considering that the Poisson's ratio of Ge  $\nu \sim 0.271$  [72], the parallel distortion  $\varepsilon_{\parallel}^{exp}$  of the Ge lattice was determined using eq. 3 [73].

$$\varepsilon_{\parallel} = \frac{-\varepsilon_{\perp}(1-\nu)}{2\nu} \quad (3)$$

$\varepsilon_{\parallel}^{exp} = -0.0024$  corresponding to  $a_{\parallel}^{exp} = 0.564$  nm (eq. 2), and thus, corresponding to a relative relaxation rate  $R = 95.5\%$  (eq. 4).

$$R = \frac{a_{\parallel} - a_{sub}}{a_{rel} - a_{sub}} \times 100 \quad (4)$$

The Ge film is significantly relaxed and should contain a high concentration of dislocations [52-62, 64-74].

Fig. 8a presents an SEM image of the Ge layer surface. A structure made of undulations in quasi-perpendicular directions is observed. Each squared structure seems to be surrounding a depression (hole?) in the layer, with a surface density  $\sim 1.2 \times 10^{11} \text{ cm}^{-2}$ . This structure is more difficult to observe in AFM images acquired on the same sample (fig. 8b). AFM images show circular and elongated islands with typical sizes (length  $\times$  width) of (100 nm  $\times$  25 nm).

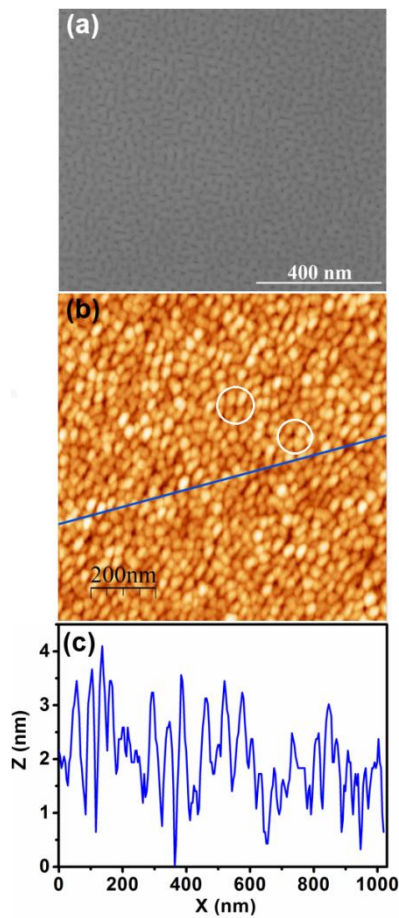


**FIG. 8.** Measurements performed on the surface of a 100 nm-thick Ge film deposited at  $T = 633 \text{ K}$  on Si(001): a) SEM image, b) AFM image, and c) AFM profile measured along the line presented in b).

The height of these islands varies typically between 1 and 3 nm (fig. 8c), and the RMS of the surface is  $\sim 0.71 \text{ nm}$ , which are significantly smaller than the thickness of the film. Similar to the

SEM images, depressions ( $\sim 3$  nm) surrounded by three to five islands are also observed (white circle in [fig. 8b](#)). The surface structure displayed in the SEM and AFM images has been also observed by Zhang et al. [\[75\]](#) on the surface of Sn-rich  $\text{Ge}_{1-x}\text{Sn}_x$  layers grown by MBE on Ge(001) substrates at  $T = 473$  K. They interpreted this surface structure as the formation of Sn islands on the  $\text{Ge}_{1-x}\text{Sn}_x$  layer surface due to Ge/Sn phase separation. However, in our case, the same structure is found on the surface of the pure Ge buffer, and thus cannot be attributed to Sn. This structure should be related to stress relaxation through elastic and plastic relaxation mechanisms. For example, similar surface states can be observed on Si(Ge) layers grown in epitaxy on Si(001) [\[73-76\]](#). The layers studied by Zhang et al. were shown to be partially relaxed and to contain threading dislocations. Considering the high relaxation level of the Ge layer, this structure should be related to both the weak residual epitaxial stress located in the film, and threading dislocations. In the case of Sn-rich  $\text{Ge}_{1-x}\text{Sn}_x$  layers with low residual strain grown by low-pressure CVD on a Ge buffer grown on Si(001), Nicolas et al. [\[77\]](#) showed thanks to APT measurements that quasi-vertical dislocation lines are passing through the  $\text{Ge}_{1-x}\text{Sn}_x$  layer up to the surface. The depressions observed on the film surface could correspond to similar dislocations reaching the surface and locally modifying the elastic strain, promoting the formation of several island-like ripples around the end of the dislocation line. In this case, the density of the surface depressions ( $1.2 \times 10^{11} \text{ cm}^{-2}$ ) should correspond to the threading dislocation density in the Ge buffer. **The presence of a surface structure on a buffer layer is not desired, as this structure may prevent the epitaxial growth of a following film and can promote the formation of structural defects at the buffer/film interface. However, in the present case, the surface roughness of the Ge buffer is very low ( $\sim 5$  Ge atomic steps in the (001) direction), and**

such a Ge buffer can be used as virtual substrate to grow pseudo-coherent Sn-rich  $\text{Ge}_{1-x}\text{Sn}_x$  layers, as reported in the case of CVD and MBE growth [54-62, 65-74].

### 3.3. Ge(Sn) single crystal growth

Fig. 9 presents X-ray diffractograms measured at RT on different 100 nm-thick  $\text{Ge}_{0.83}\text{Sn}_{0.17}$  films grown on the Ge buffer in different conditions. The diffractogram (a) corresponds to a  $\text{Ge}_{0.83}\text{Sn}_{0.17}$  film deposited at the same temperature as the Ge buffer without growth interruption. The chosen growth temperature  $T = 633$  K is 100 K lower than the  $\text{Ge}_{0.83}\text{Sn}_{0.17}$  crystallization temperature determined in the XRD *in situ* ramp annealing experiments ( $T = 733$  K), aiming to increase Sn incorporation, but is 200 K higher than the growth temperature used in former studies ( $T = 423$  K) for growing  $\text{Ge}_{0.94}\text{Sn}_{0.06}$  layers by sputtering, aiming to improve the layer crystalline properties. This temperature is actually in the range used to grow Sn-rich  $\text{Ge}_{1-x}\text{Sn}_x$  layers by CVD or MBE.

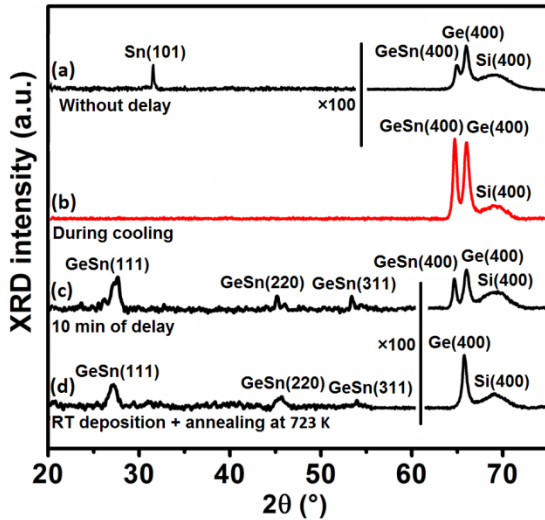
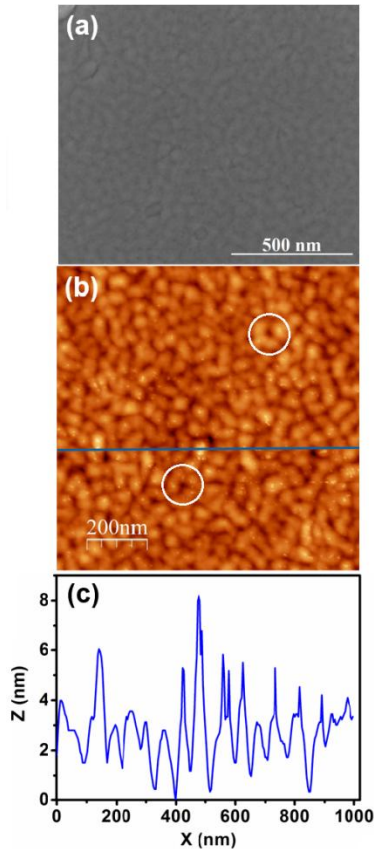


FIG. 9. X-ray diffractograms measured at RT on different 100 nm-thick  $\text{Ge}_{0.83}\text{Sn}_{0.17}$  films grown in different conditions on a 100 nm-thick Ge buffer grown at  $T = 633$  K on Si(001): a) deposition at the same temperature as the Ge buffer without growth interruption, b) deposition without growth interruption but stopping sample heating before  $\text{Ge}_{0.83}\text{Sn}_{0.17}$  deposition, c) deposition after stopping sample heating at the end of the Ge buffer deposition and with a growth interruption of 10 min before  $\text{Ge}_{0.83}\text{Sn}_{0.17}$  deposition, and d) crystallization of an amorphous  $\text{Ge}_{0.83}\text{Sn}_{0.17}$  film deposited at RT on the Ge buffer.

The (004) diffraction peak is the only one corresponding to the diamond structure detected for the Si substrate, as well as for the Ge and  $\text{Ge}_{1-x}\text{Sn}_x$  layers, displaying the pseudo-coherent relation between the substrate and the two stacked layers. However, one can note that the  $\text{Ge}_{1-x}\text{Sn}_x(400)$  diffraction peak is less intense than that of the Ge(400). A small diffraction peak corresponding to  $\beta\text{-Sn}(101)$  is also detected, meaning that Sn droplets are probably present on the sample surface (Fig. 3). The formation of the phase  $\beta\text{-Sn}$  can be suppressed using a modified growth process consisting of switching off the sample heater before growing the  $\text{Ge}_{1-x}\text{Sn}_x$  layer, without growth interruption between the Ge buffer and the  $\text{Ge}_{1-x}\text{Sn}_x$  layer. In this case, XRD measurements (diffractogram (b) in Fig. 9) show no sign of the  $\beta\text{-Sn}$  phase, and the  $\text{Ge}_{1-x}\text{Sn}_x(400)$  and Ge(400) diffraction peak intensities are similar. The diffractogram (c) shown in Fig. 9 was acquired on a sample for which the sample heater was switched off after the growth of the Ge buffer and a growth interruption of 10 min was performed before  $\text{Ge}_{1-x}\text{Sn}_x$  growth. The  $\beta\text{-Sn}$  phase is not detected in this case, but the  $\text{Ge}_{1-x}\text{Sn}_x(400)$  peak intensity is smaller than the Ge(400) peak intensity, and additional  $\text{Ge}_{1-x}\text{Sn}_x$  diffraction peaks are observed, corresponding to the three diamond lattice orientations (111), (220), and (311), usually detected for Ge and  $\text{Ge}_{1-x}\text{Sn}_x$  layers crystallized from an amorphous layer deposited on Si(001) (Figs. 1b, 5a, and 7). Obviously, the  $\text{Ge}_{1-x}\text{Sn}_x$  layer grew in pseudo-epitaxy on the Ge buffer at the beginning, but due to the temperature decrease, the end of the  $\text{Ge}_{1-x}\text{Sn}_x$  growth promoted the formation of a polycrystalline layer. However, according to the significant difference of diffraction peak intensity, the top polycrystalline layer should be significantly thinner than the monocrystalline layer in contact with the Ge buffer. The last diffractogram (d) in Fig. 9 was acquired after the crystallization of an amorphous  $\text{Ge}_{0.83}\text{Sn}_{0.17}$  film deposited at RT on the Ge buffer. In this case,

the Ge buffer is pseudo-coherent with the Si(001) substrate, but the  $\text{Ge}_{1-x}\text{Sn}_x$  film is entirely polycrystalline and the  $\text{Ge}_{1-x}\text{Sn}_x(400)$  peak characteristic of epitaxial growth is not detected.

As expected, the growth of a pseudo-coherent  $\text{Ge}_{1-x}\text{Sn}_x$  layer on Si(001) without the formation of the  $\beta$ -Sn phase is highly dependent on kinetics, and growth conditions generally need to be determined empirically. Fig. 10 shows SEM and AFM measurements performed on the surface of the  $\text{Ge}_{1-x}\text{Sn}_x$  layer coherently grown on the Ge buffer (diffractogram (b) in Fig. 9).



**FIG. 10.** Analyses performed on the surface of a 100 nm-thick  $\text{Ge}_{0.83}\text{Sn}_{0.17}$  film deposited on a 100 nm-thick Ge buffer grown at  $T = 633$  K on Si(001) in the conditions corresponding to Fig. 9b (no growth interruption, sample heater off): a) SEM image, b) AFM image, and c) AFM profile measured along the line presented in b).

A surface structure is observed similar to that displayed on the Ge buffer before  $\text{Ge}_{1-x}\text{Sn}_x$  deposition, in agreement with the observations of Zhang et al. [75]. The pattern is less organized than that on the Ge buffer surface. The ripples/islands exhibit a similar average height  $\sim 3$  nm (Fig. 10c), but they are larger with an average width  $\sim 75$  nm (Figs. 10a and 10b). The RMS of

the surface is  $\sim 1.24$  nm. One can note that 3 nm-high islands on the Ge surface should have been easily covered with the 100 nm-thick  $\text{Ge}_{1-x}\text{Sn}_x$  layer. The fact that this topography is also observed on the  $\text{Ge}_{1-x}\text{Sn}_x$  surface is thus in agreement with the effect of extended defects, such as dislocations, which can propagate in the  $\text{Ge}_{1-x}\text{Sn}_x$  layer from its pseudo-coherent interface with the Ge buffer up to the surface. The surface density of the depressions surrounded with islands is reduced to  $\sim 3.3 \times 10^{10} \text{ cm}^{-2}$  on the  $\text{Ge}_{1-x}\text{Sn}_x$  surface. Consequently, the  $\text{Ge}_{1-x}\text{Sn}_x$  layer may contain a threading dislocation density almost one order of magnitude smaller than that of the Ge buffer. This might be related to the lower misfit between  $\text{Ge}_{1-x}\text{Sn}_x$  and Ge (about 1.5%) than between Ge and Si (about 4%).

However, the precise determination of the misfit requires knowledge of the composition of Sn in  $\text{Ge}_{1-x}\text{Sn}_x$ . **Fig. 11a** presents the Sn and Ge atomic distributions determined by APT in the  $\text{Ge}_{1-x}\text{Sn}_x$  layer. The Sn and Ge distributions (solid symbols) follow random distributions (solid lines), and are centered on 10 at% and 90 at% for Sn and Ge, respectively. Thus, the film corresponds to a  $\text{Ge}_{0.9}\text{Sn}_{0.1}$  solid solution free of Sn clusters. Interestingly, no contaminants are detected in the  $\text{Ge}_{0.9}\text{Sn}_{0.1}$  layer. Indeed, **Fig. 11b** shows part of the mass spectrum corresponding to the  $\text{Ge}_{0.9}\text{Sn}_{0.1}$  layer.

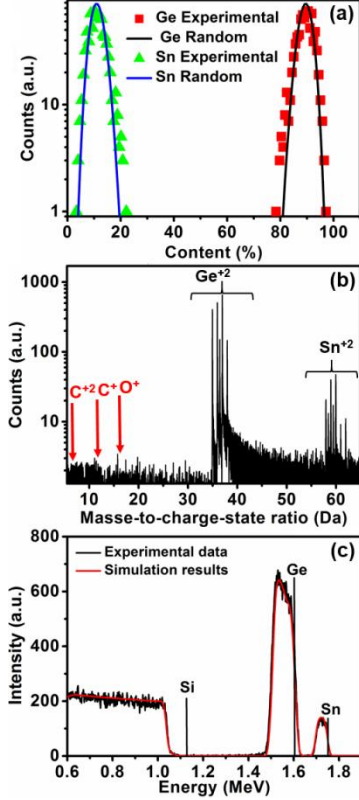


**FIG. 11.** Chemical characterization of the 100 nm-thick  $\text{Ge}_{0.83}\text{Sn}_{0.17}$  film deposited on a 100 nm-thick Ge buffer grown at  $T = 633$  K on Si(001) in the conditions corresponding to Fig. 9b (no growth interruption, sample heater off): a) Ge and Sn atomic distributions determined by APT in the  $\text{Ge}_{1-x}\text{Sn}_x$  layer (solid symbols) compared to random distribution (solid lines) centered on 90 and 10 at%, respectively, b) part of the mass spectrum acquired by APT in the  $\text{Ge}_{1-x}\text{Sn}_x$  layer, and d) RBS measurements performed on the same sample (black) and simulations (red solid line) corresponding to the structure 100 nm-thick  $\text{Ge}_{0.0}\text{Sn}_{0.1}$  /100 nm-thick Ge /Si(001).

The impurities C and O usually incorporated in sputtered layers are not detected, meaning that their concentrations are lower than  $2 \times 10^{19}$  at  $\text{cm}^{-3}$  ( $\sim 0.04$  at%) in the film [78]. The Sn composition determined by APT is in agreement with RBS measurements performed on the same sample (Fig. 11c). Furthermore, the RBS measurements are consistent with the stack of a 100 nm-thick  $\text{Ge}_{0.9}\text{Sn}_{0.1}$  layer and a 100 nm-thick Ge layer on the Si substrate. However, one can note that the Sn concentration of this film is significantly lower than that of the expected  $\text{Ge}_{0.83}\text{Sn}_{0.17}$  film, corresponding to Ge and Sn fluxes used during growth. Since no Sn cluster was detected by APT in the  $\text{Ge}_{0.9}\text{Sn}_{0.1}$  layer, this lack of Sn should be mainly due to Sn desorption from the sample surface during growth. Indeed, the growth was performed at a temperature about 100 K higher than the Sn bulk melting temperature, at a pressure  $P \sim 3 \times 10^{-3}$  mbar of Ar. The lattice parameter of the  $\text{Ge}_{0.9}\text{Sn}_{0.1}$  layer in the direction perpendicular to the sample surface was found to be  $a_{\perp}^{\text{exp}} = 0.576$  nm from the angle of the  $\text{Ge}_{1-x}\text{Sn}_x(400)$  diffraction peak in the

diffractogram (b) in Fig. 9. Considering that  $a_{0.1}^{GeSn} = 0.574$  nm (eq. 1), the perpendicular distortion of the  $Ge_{0.9}Sn_{0.1}$  lattice parameter was found to be  $\varepsilon_{\perp}^{exp} = 0.0035$  (eq. 2).

$$\nu_x^{GeSn} = (1 - x)\nu_{Ge} + x\nu_{Sn} \quad (5)$$

According to eq. 5 [72], the Poisson's ratio of  $Ge_{0.9}Sn_{0.1}$  is  $\nu_{0.1}^{GeSn} = 0.280$  ( $\nu_{Ge} = 0.271$  and  $\nu_{Sn} = 0.360$  [72]), leading to  $\varepsilon_{//}^{exp} = -0.0045$  (eq. 3) and  $a_{//}^{exp} = 0.571$  nm (eq. 2). Consequently, the relative relaxation rate of the  $Ge_{0.9}Sn_{0.1}$  film compared to that of the Si substrate is  $R = 90.3\%$  (eq. 4). The  $Ge_{0.9}Sn_{0.1}$  film is significantly relaxed, but not as relaxed as the Ge buffer, which is in agreement with a lower dislocation density in the  $Ge_{0.9}Sn_{0.1}$  layer. The resistivity of the undoped  $Ge_{0.9}Sn_{0.1}$  film was measured at RT. It was found to be  $\rho_{0.1}^{GeSn} = 8 \times 10^{-4}$   $\Omega$  cm. For comparison, the resistivity of undoped monocrystalline Ge at RT is  $\rho_{Ge} \sim 50$   $\Omega$  cm [79].

Despite the unusual deposition technique employed for semiconductor growth, and the significant threading dislocation density probably contained in the layers, the resistivity of the  $Ge_{0.9}Sn_{0.1}$  film is found to be four orders of magnitude lower than that of Ge. Magnetron sputtering can be used to grow a pseudo-coherent  $Ge_{0.9}Sn_{0.1}$  film on Si(001) at a relatively high temperature ( $T = 633$  K), displaying a high level of relaxation ( $R = 90.3\%$ ) and relatively low impurity concentrations ( $< 2 \times 10^{19}$  at  $cm^{-3}$ ), exhibiting interesting electrical properties ( $\rho_{0.1}^{GeSn} = 8 \times 10^{-4}$   $\Omega$  cm).

#### 4. Conclusion

Magnetron sputtering growth of  $Ge_{1-x}Sn_x$  layers ( $x > 0.6$ ) on Si(001) was performed at similar temperatures as usually used for MBE and CVD growth. XRD *in situ* measurements

clearly evidenced the competition between Sn incorporation and crystal growth. The high crystallization temperature of  $\text{Ge}_{1-x}\text{Sn}_x$ , compared to the atomic diffusion kinetic and to the Sn melting temperature, drastically limits the fabrication of crystalline Sn-rich  $\text{Ge}_{1-x}\text{Sn}_x$  films. Furthermore, the crystallization of an amorphous  $\text{Ge}_{1-x}\text{Sn}_x$  layer deposited directly on a clean Si(001) substrate, or on a Ge buffer grown on the Si(001) substrate, does not allow the growth of a pseudo-coherent  $\text{Ge}_{1-x}\text{Sn}_x$  layer, probably due to crystal nucleation starting at the surface of the amorphous  $\text{Ge}_{1-x}\text{Sn}_x$  layer instead of at the  $\text{Ge}_{1-x}\text{Sn}_x/\text{Si}(001)$  or  $\text{Ge}_{1-x}\text{Sn}_x/\text{Ge}(001)$  interface. The Ge buffer and the  $\text{Ge}_{1-x}\text{Sn}_x$  layer must be grown at a temperature allowing for crystal growth and dislocation nucleation without significant atomic transport, in order to grow a monocrystalline layer without Ge/Sn phase separation. This temperature can be significantly lower than the  $\text{Ge}_{1-x}\text{Sn}_x$  crystallization temperature, as the nucleation process is unnecessary when the layers are grown on a single crystal. The low-cost and CMOS-compatible magnetron sputtering technique can be used to grow, at similar temperature as for CVD or MBE growth, relaxed Sn-rich  $\text{Ge}_{1-x}\text{Sn}_x$  layers with  $x \geq 0.1$ , displaying low impurity concentrations and reasonable electrical properties. While Sn incorporation is mainly limited by Ge/Sn phase separation kinetics during  $\text{Ge}_{1-x}\text{Sn}_x$  crystallization, Sn surface desorption appears as the main limiting phenomenon during growth at temperatures lower than the crystallization temperature.

## **Acknowledgements**

This work was supported by the French-Algerian cooperation program PROFAS B+. The Ion Technology Centre ITC, Uppsala University, Sweden, is acknowledged for the RBS facilities.

## References

- [1] J. W. Jeong *et al.*, “Tunnelling-based ternary metal–oxide–semiconductor technology,” *Nat. Electron.*, vol. 2, no. 7, pp. 307–312, Jul. 2019, doi: 10.1038/s41928-019-0272-8.
- [2] A. L. Robinson, “CMOS Future for Microelectronic Circuits: Low power consumption of complementary metal-oxide-semiconductor integrated circuits drives next stage of ultraminiaturization,” *Science*, vol. 224, no. 4650, pp. 705–707, May 1984, doi: 10.1126/science.224.4650.705.
- [3] P. Arunkumar, S. K. Kuanr, and K. S. Babu, “Thin Film: Deposition, Growth Aspects, and Characterization,” in *Thin Film Structures in Energy Applications*, S. Babu Krishna Moorthy, Ed. Cham: Springer International Publishing, 2015, pp. 1–49.
- [4] R. Pillarisetty, “Academic and industry research progress in germanium nanodevices,” *Nature*, vol. 479, no. 7373, pp. 324–328, Nov. 2011, doi: 10.1038/nature10678.
- [5] C. Chang, “Formation of copper silicides from Cu(100)/Si(100) and Cu(111)/Si(111) structures,” *J. Appl. Phys.*, vol. 67, no. 1, pp. 566–569, Jan. 1990, doi: 10.1063/1.345194.
- [6] D. Mangelinck *et al.*, “Three-dimensional composition mapping of NiSi phase distribution and Pt diffusion via grain boundaries in Ni<sub>2</sub>Si,” *Scr. Mater.*, vol. 62, no. 8, pp. 568–571, Apr. 2010, doi: 10.1016/j.scriptamat.2009.12.044.
- [7] B. Radisavljevic, A. Radenovic, J. Brivio, V. Giacometti, and A. Kis, “Single-layer MoS<sub>2</sub> transistors,” *Nat. Nanotechnol.*, vol. 6, no. 3, pp. 147–150, Mar. 2011, doi: 10.1038/nnano.2010.279.
- [8] Yee-Chia Yeo *et al.*, “Dual-metal gate CMOS technology with ultrathin silicon nitride gate dielectric,” *IEEE Electron Device Lett.*, vol. 22, no. 5, pp. 227–229, May 2001, doi: 10.1109/55.919237.
- [9] T. Nagatsuma, G. Ducournau, and C. C. Renaud, “Advances in terahertz communications accelerated by photonics,” *Nat. Photonics*, vol. 10, no. 6, pp. 371–379, Jun. 2016, doi: 10.1038/nphoton.2016.65.
- [10] Y. A. Vlasov, “Silicon CMOS-integrated nano-photonics for computer and data communications beyond 100G,” *IEEE Commun. Mag.*, vol. 50, no. 2, pp. s67–s72, Feb. 2012, doi: 10.1109/MCOM.2012.6146487.
- [11] O. Graydon, “The data centre challenge,” *Nat. Photonics*, vol. 9, no. 10, pp. 637–638, Oct. 2015, doi: 10.1038/nphoton.2015.186.
- [12] G. T. Reed, G. Mashanovich, F. Y. Gardes, and D. J. Thomson, “Silicon optical modulators,” *Nat. Photonics*, vol. 4, no. 8, pp. 518–526, Aug. 2010, doi: 10.1038/nphoton.2010.179.
- [13] M. Hochberg and T. Baehr-Jones, “Towards fabless silicon photonics,” *Nat. Photonics*, vol. 4, no. 8, pp. 492–494, Aug. 2010, doi: 10.1038/nphoton.2010.172.
- [14] X. Chen, C. Li, and H. K. Tsang, “Device engineering for silicon photonics,” *NPG Asia Mater.*, vol. 3, no. 1, pp. 34–40, Jan. 2011, doi: 10.1038/asiamat.2010.194.
- [15] M. Cazzanelli *et al.*, “Second-harmonic generation in silicon waveguides strained by silicon nitride,” *Nat. Mater.*, vol. 11, no. 2, pp. 148–154, Feb. 2012, doi: 10.1038/nmat3200.
- [16] C. Lacava *et al.*, “Si-rich Silicon Nitride for Nonlinear Signal Processing Applications,” *Sci. Rep.*, vol. 7, no. 1, pp. 1–13, Feb. 2017, doi: 10.1038/s41598-017-00062-6.
- [17] Y. Kim, M. Takenaka, T. Osada, M. Hata, and S. Takagi, “Strain-induced enhancement of plasma dispersion effect and free-carrier absorption in SiGe optical modulators,” *Sci. Rep.*, vol. 4, no. 1, pp. 1–6, Apr. 2014, doi: 10.1038/srep04683.

- [18] J. Michel, J. Liu, and L. C. Kimerling, “High-performance Ge-on-Si photodetectors,” *Nat. Photonics*, vol. 4, no. 8, pp. 527–534, Aug. 2010, doi: 10.1038/nphoton.2010.157.
- [19] I. Stavarache *et al.*, “SiGe nanocrystals in SiO<sub>2</sub> with high photosensitivity from visible to short-wave infrared,” *Sci. Rep.*, vol. 10, no. 1, pp. 1–9, Feb. 2020, doi: 10.1038/s41598-020-60000-x.
- [20] H. Cong *et al.*, “Silicon Based GeSn p-i-n Photodetector for SWIR Detection,” *IEEE Photonics J.*, vol. 8, no. 5, pp. 1–6, Oct. 2016, doi: 10.1109/JPHOT.2016.2607687.
- [21] M. Oehme *et al.*, “GeSn Heterojunction LEDs on Si Substrates,” *IEEE Photonics Technol. Lett.*, vol. 26, no. 2, pp. 187–189, Jan. 2014, doi: 10.1109/LPT.2013.2291571.
- [22] A. Elbaz *et al.*, “Ultra-low-threshold continuous-wave and pulsed lasing in tensile-strained GeSn alloys,” *Nat. Photonics*, pp. 1–8, Mar. 2020, doi: 10.1038/s41566-020-0601-5.
- [23] S. Ghosh *et al.*, “Metal-Semiconductor-Metal GeSn Photodetectors on Silicon for Short-Wave Infrared Applications,” *Micromachines*, vol. 11, no. 9, p. 795, Aug. 2020, doi: 10.3390/mi11090795.
- [24] K. Choe, M. R. Hogsed, N. Miguel, J. W. McClory, and J. Kouvetakis, “Displacement Damage Effects in Germanium Tin LEDs,” vol. 38, no. 1, p. 8, 2020.
- [25] Y. Zhou *et al.*, “Optically Pumped GeSn Lasers Operating at 270 K with Broad Waveguide Structures on Si,” *ACS Photonics*, vol. 6, no. 6, pp. 1434–1441, Jun. 2019, doi: 10.1021/acsp Photonics.9b00030.
- [26] A. Elbaz *et al.*, “Reduced Lasing Thresholds in GeSn Microdisk Cavities with Defect Management of the Optically Active Region,” *ACS Photonics*, p. acsp Photonics.0c00708, Sep. 2020, doi: 10.1021/acsp Photonics.0c00708.
- [27] K. P. Homewood and M. A. Lourenço, “The rise of the GeSn laser,” *Nature Photon.*, Vol. 9, pp. 78–79, February 2015, doi: 10.1038/nphoton.2015.1.
- [28] K. Moto, R. Yoshimine, T. Suemasu, K. Toko, “Improving carrier mobility of polycrystalline Ge by Sn doping,” *Sci. Rep.*, vol. 8, p. 14832, October 2018, doi: 10.1038/s41598-018-33161-z.
- [29] C. Xu, X. Gong, M. Miyao, and T. Sadoh, “Enhanced mobility of Sn-doped Ge thin-films ( $\leq 50$  nm) on insulator for fully depleted transistors by nucleation-controlled solid-phase crystallization,” *Appl. Phys. Lett.*, vol. 115, no. 4, p. 042101, Jul. 2019, doi: 10.1063/1.5096798.
- [30] Roucka *et al.* patent US2014/0053894A1, Feb. 2014.
- [31] H. J. Möller and V. Schlichting, “Measurement and calculation of the carrier concentration in polycrystalline germanium thin films,” *Springer Proc. Phys.*, vol. 35, pp. 326–331, 1989.
- [32] S. Wirths *et al.*, “Lasing in direct-bandgap GeSn alloy grown on Si,” *Nat. Photonics*, vol. 9, no. 2, pp. 88–92, Feb. 2015, doi: 10.1038/nphoton.2014.321.
- [33] J. Song, X. Zhao, X. Wu, and R. Xuan, “High rectification efficiency direct bandgap Ge<sub>1-x</sub>Sn<sub>x</sub> Schottky diode for microwave wireless power transfer,” *Appl. Phys. A*, vol. 125, no. 10, p. 719, Sep. 2019, doi: 10.1007/s00339-019-3002-1.
- [34] S. Prucnal *et al.*, “Ex situ n<sup>+</sup> doping of GeSn alloys via non-equilibrium processing,” *Semicond. Sci. Technol.*, vol. 33, no. 6, p. 065008, May 2018, doi: 10.1088/1361-6641/aabe05.
- [35] “Binary Alloy Phase Diagrams, 2nd Edition - ASM International.”  
[https://www.asminternational.org/online-catalog/alloy-phase-diagrams/-/journal\\_content/56/10192/57718G/PUBLICATION](https://www.asminternational.org/online-catalog/alloy-phase-diagrams/-/journal_content/56/10192/57718G/PUBLICATION) (accessed Apr. 29, 2020).
- [36] R. W. Olesinski and G. J. Abbaschian, “The Ge–Sn (Germanium–Tin) system,” *Bull. Alloy Phase Diagr.*, vol. 5, no. 3, pp. 265–271, Jun. 1984, doi: 10.1007/BF02868550.

- [37] H. Groiss *et al.*, “Free-running Sn precipitates: an efficient phase separation mechanism for metastable Ge  $1-x$  Sn  $x$  epilayers,” *Sci. Rep.*, vol. 7, no. 1, pp. 1–12, Nov. 2017, doi: 10.1038/s41598-017-16356-8.
- [38] “KittelCharles-IntroductionToSolidStatePhysics8ThEd.pdf” .
- [39] S. d. Allen, “Laser chemical vapor deposition: A technique for selective area deposition,” *J. Appl. Phys.*, vol. 52, no. 11, pp. 6501–6505, Nov. 1981, doi: 10.1063/1.328600.
- [40] M. B. Panish, “Molecular Beam Epitaxy,” *Science*, vol. 208, no. 4446, pp. 916–922, May 1980, doi: 10.1126/science.208.4446.916.
- [41] S. Lee *et al.*, “Fabrication of high-quality single-crystal Cu thin films using radio-frequency sputtering,” *Sci. Rep.*, vol. 4, no. 1, pp. 1–6, Aug. 2014, doi: 10.1038/srep06230.
- [42] R. Xu, W. Li, J. He, K.-C. Qi, and Y.-D. Jiang, “Structural and photoelectric properties of a-SiGe:H thin films with varied Ge prepared by PECVD,” in *2011 Asia Communications and Photonics Conference and Exhibition (ACP)*, Nov. 2011, pp. 1–7, doi: 10.1117/12.904214.
- [43] D. Zhang, L. Jin, Y. Liao, H. Zhang, and J. Kolodzey, “Microstructure and optic-electric performance of SiGe/Si heterostructures,” in *2016 IEEE International Nanoelectronics Conference (INEC)*, May 2016, pp. 1–2, doi: 10.1109/INEC.2016.7589384.
- [44] M. Mysliwiec, M. Sochacki, R. Kisiel, M. Guziewicz, and M. Wzorek, “TiAl-based ohmic contacts on p-type SiC,” in *Proceedings of the 2011 34th International Spring Seminar on Electronics Technology (ISSE)*, May 2011, pp. 68–72, doi: 10.1109/ISSE.2011.6053552.
- [45] K. Buchholt *et al.*, “Ohmic contact properties of magnetron sputtered Ti<sub>3</sub>SiC<sub>2</sub> on n- and p-type 4H-silicon carbide,” *Appl. Phys. Lett.*, vol. 98, no. 4, p. 042108, Jan. 2011, doi: 10.1063/1.3549198.
- [46] J. Zheng *et al.*, “GeSn p-i-n photodetectors with GeSn layer grown by magnetron sputtering epitaxy,” *Appl. Phys. Lett.*, vol. 108, no. 3, p. 033503, Jan. 2016, doi: 10.1063/1.4940194.
- [47] L. Zhang *et al.*, “Raman scattering study of amorphous GeSn films and their crystallization on Si substrates,” *J. Non-Cryst. Solids*, vol. 448, pp. 74–78, Sep. 2016, doi: 10.1016/j.jnoncrysol.2016.07.007.
- [48] H. Mahmodi, M. R. Hashim, and U. Hashim, “Formation of nanocrystalline GeSn thin film on Si substrate by sputtering and rapid thermal annealing,” *Superlattices Microstruct.*, vol. 98, pp. 235–241, Oct. 2016, doi: 10.1016/j.spmi.2016.08.030.
- [49] H. Mahmodi, M. Hashim, T. Soga, S. Alrokayan, H. Khan, and M. Rusop, “Synthesis of Ge<sub>1-x</sub>Sn<sub>x</sub> Alloy Thin Films by Rapid Thermal Annealing of Sputtered Ge/Sn/Ge Layers on Si Substrates,” *Materials*, vol. 11, no. 11, p. 2248, Nov. 2018, doi: 10.3390/ma11112248.
- [50] H. P. Ladrón de Guevara, A. G. Rodríguez, H. Navarro-Contreras, and M. A. Vidal, “Ge<sub>1-x</sub>Sn<sub>x</sub> alloys pseudomorphically grown on Ge(001),” *Appl. Phys. Lett.*, vol. 83, no. 24, pp. 4942–4944, Dec. 2003, doi: 10.1063/1.1634374.
- [51] L. Qian *et al.*, “GeSn/GaAs Hetero-Structure by Magnetron Sputtering,” *IEEE J. Quantum Electron.*, vol. 56, no. 2, pp. 1–5, Apr. 2020, doi: 10.1109/JQE.2019.2963057.
- [52] J. Zheng *et al.*, “Growth of Crystalline Ge<sub>1-x</sub>Sn<sub>x</sub> Films on Si (100) by Magnetron Sputtering,” *ECS Solid State Lett.*, vol. 3, no. 9, p. P111, Jul. 2014, doi: 10.1149/2.0081409ssl.
- [53] N. Taoka *et al.*, “Electrical and optical properties improvement of GeSn layers formed at high temperature under well-controlled Sn migration,” *Mater. Sci. Semicond. Process.*, vol. 57, pp. 48–53, Jan. 2017, doi: 10.1016/j.mssp.2016.09.040.

- [54] B. R. Conley *et al.*, “Temperature dependent spectral response and detectivity of GeSn photoconductors on silicon for short wave infrared detection,” *Opt. Express*, vol. 22, no. 13, pp. 15639–15652, Jun. 2014, doi: 10.1364/OE.22.015639.
- [55] X. Zhang *et al.*, “Crystal Quality Improvement of GeSn Alloys by Thermal Annealing,” *ECS Solid State Lett.*, vol. 3, no. 10, p. P127, Aug. 2014, doi: 10.1149/2.0101410ssl.
- [56] S. A. Ghetmiri *et al.*, “Direct-bandgap GeSn grown on silicon with 2230 nm photoluminescence,” *Appl. Phys. Lett.*, vol. 105, no. 15, p. 151109, Oct. 2014, doi: 10.1063/1.4898597.
- [57] T. T. Tran *et al.*, “Ion beam synthesis and photoluminescence study of supersaturated fully-relaxed Ge-Sn alloys,” *Mater. Sci. Eng. B*, vol. 262, p. 114702, Dec. 2020, doi: 10.1016/j.mseb.2020.114702.
- [58] T. T. Tran *et al.*, “Ion beam synthesis and photoluminescence study of supersaturated fully-relaxed Ge-Sn alloys,” *Mater. Sci. Eng. B*, vol. 262, p. 114702, Dec. 2020, doi: 10.1016/j.mseb.2020.114702.
- [59] U. Holzwarth and N. Gibson, “The Scherrer equation versus the ‘Debye-Scherrer equation,’” *Nat. Nanotechnol.*, vol. 6, no. 9, pp. 534–534, Sep. 2011, doi: 10.1038/nnano.2011.145.
- [60] F. Gencarelli *et al.*, “Crystalline Properties and Strain Relaxation Mechanism of CVD Grown GeSn,” *ECS J. Solid State Sci. Technol.*, vol. 2, no. 4, p. P134, Jan. 2013, doi: 10.1149/2.011304jss.
- [61] M. Kim *et al.*, “Polycrystalline GeSn thin films on Si formed by alloy evaporation,” *Appl. Phys. Express*, vol. 8, no. 6, p. 061301, May 2015, doi: 10.7567/APEX.8.061301.
- [62] M. Liu and R. Y. Wang, “Size-Dependent Melting Behavior of Colloidal In, Sn and Bi Nanocrystals,” *Sci. Rep.*, vol. 5, no. 1, pp. 1–9, Nov. 2015, doi: 10.1038/srep16353.
- [63] A. Portavoce, O. Abbes, Y. Rudzevich, L. Chow, V. Le Thanh, C. Girardeaux, “Manganese diffusion in monocrystalline germanium”, *Scripta Mater.*, vol. 67, pp. 269–272, May 2012, doi: 10.1016/j.scriptamat.2012.04.038.
- [64] A. Chronos and H. Bracht, “Diffusion of n-type dopants in germanium”, *Appl. Phys. Rev.*, vol. 1, p. 011301, January 2014, doi: 10.1063/1.4838215.
- [65] K. Toko, N. Oya, N. Saitoh, N. Yoshizawa, and T. Suemasu, “70 °C synthesis of high-Sn content (25%) GeSn on insulator by Sn-induced crystallization of amorphous Ge,” *Appl. Phys. Lett.*, vol. 106, no. 8, p. 082109, Feb. 2015, doi: 10.1063/1.4913744.
- [66] J.M. Bermond, J.J. Métois, X. Egéa, F. Floret, “The equilibrium shape of silicon”, *Surface Science*, vol. 330, pp. 48-60, 1995, SSD1 0039-6028(95)00230-8
- [67] A. Portavoce, A. Ronda, I. Berbezier, “Sb-surfactant mediated growth of Ge nanostructures”, *Mat. Sci. Eng. B*, vol. 89, pp. 205–210, 2002, PII: S0921-5107(01)00853-4.
- [68] A. Portavoce, R. Hull, M. C. Reuter, M. Copel, and F. M. Ross, “Control of homoepitaxial Si nanostructures by locally modified surface reactivity”, *Appl. Phys. Lett.*, vol. 92, p. 053106, Feb. 2008, doi: 10.1063/1.2841673.
- [69] Yu. G. Sadofyev, V. P. Martovitsky, M. A. Bazalevsky, A. V. Klekovkin, D. V. Averyanov, and I. S. Vasil’evskii, “Ge/GeSn heterostructures grown on Si (100) by molecular-beam epitaxy,” *Semiconductors*, vol. 49, no. 1, pp. 124–129, Jan. 2015, doi: 10.1134/S1063782615010248.
- [70] P. Moontragoon, R. A. Soref, and Z. Ikonic, “The direct and indirect bandgaps of unstrained SixGe1–x–ySny and their photonic device applications,” *J. Appl. Phys.*, vol. 112, no. 7, p. 073106, Oct. 2012, doi: 10.1063/1.4757414.

- [71] S. Wirths *et al.*, “Tensely strained GeSn alloys as optical gain media,” *Appl. Phys. Lett.*, vol. 103, no. 19, p. 192110, Nov. 2013, doi: 10.1063/1.4829360.
- [72] J. Aubin *et al.*, “Impact of thickness on the structural properties of high tin content GeSn layers,” *J. Cryst. Growth*, vol. 473, pp. 20–27, Sep. 2017, doi: 10.1016/j.jcrysgro.2017.05.006.
- [73] I. Berbezier, A. Ronda, and A. Portavoce, “SiGe nanostructures: new insights into growth processes,” *J. Phys. Condens. Matter*, vol. 14, no. 35, pp. 8283–8331, Aug. 2002, doi: 10.1088/0953-8984/14/35/306.
- [74] S. Takeuchi, Y. Shimura, O. Nakatsuka, S. Zaima, M. Ogawa, and A. Sakai, “Growth of highly strain-relaxed Ge<sub>1-x</sub>Sn<sub>x</sub>/virtual Ge by a Sn precipitation controlled compositionally step-graded method,” *Appl. Phys. Lett.*, vol. 92, no. 23, p. 231916, Jun. 2008, doi: 10.1063/1.2945629.
- [75] Z. P. Zhang *et al.*, “Structural properties of GeSn thin films grown by molecular beam epitaxy,” *AIP Adv.*, vol. 7, no. 4, p. 045211, Apr. 2017, doi: 10.1063/1.4982245.
- [76] F. Volpi, A. Portavoce, A. Ronda, Y. Shi, J. M. Gay, and I. Berbezier, “Nucleation and evolution of Si<sub>1-x</sub>Ge<sub>x</sub> islands on Si(001),” *Thin Solid Films*, vol. 380, no. 1, pp. 46–50, Dec. 2000, doi: 10.1016/S0040-6090(00)01526-1.
- [77] J. Nicolas, S. Assali, S. Mukherjee, A. Lotnyk, and O. Moutanabbir, “Dislocation pipe diffusion and solute segregation during the growth of metastable GeSn”, *Cryst. Growth Des.*, Apr. 2020, doi: 10.1021/acs.cgd.0c00270.
- [78] M. Descoins, J. Perrin Toinin, S. Zhiou, K. Hoummada, M. Bertoglio, R. Ma, L. Chow, D. Narducci, A. Portavoce, "PdGe contact fabrication on Se-doped Ge", *Scripta Mater.*, vol. 139, pp. 104-107, June 2017, doi: 10.1016/j.scriptamat.2017.06.029.
- [79] L. H. Chan, E. I. Altman, and Y. Liang, “Development of procedures for obtaining clean, low-defect-density Ge(100) surfaces,” *J. Vac. Sci. Technol. A*, vol. 19, no. 3, pp. 976–981, May 2001, doi: 10.1116/1.1367264.

## FIGURE CAPTIONS

**FIG. 1.** a) XRD measurements performed during the *in situ* annealing of an amorphous  $\text{Ge}_{0.83}\text{Sn}_{0.17}$  film deposited on Si(001), following an average ramp of  $\sim 1 \text{ K min}^{-1}$  from 423 to  $T = 853 \text{ K}$ ; and b) diffractogram acquired at  $T = 778 \text{ K}$  during the *in situ* annealing (red line in a).

**FIG. 2.** XRD measurements performed during the *in situ* annealing of an amorphous  $\text{Ge}_{0.83}\text{Sn}_{0.17}$  film deposited on Si(001), following an average ramp of  $\sim 1 \text{ K min}^{-1}$  from 523 to  $T = 853 \text{ K}$ : a) integrated and normalized intensity of the  $\text{Ge}_{1-x}\text{Sn}_x(111)$  diffraction peak versus temperature, and b) average grain size determined from the half-maximum width of the (111) peak using the Scherrer equation (solid squares, right axis), and Sn concentration determined from the diffraction angle  $2\theta$  of the (111) peak (solid triangles, left axis).

**FIG. 3.** Analyses performed at RT on the sample that experienced the XRD *in situ* annealing presented in Fig. 1 and 2: a) X-ray diffractogram, b) SEM measurements, and c) AFM measurements.

**FIG. 4.** Cross-section TEM measurements performed on the sample that experienced the XRD *in situ* annealing presented in Fig. 1 and 2: a) STEM Dark-Field image, b) and c) High-Resolution TEM images. The inset in c) presents the local FFT obtained on the layer A.

**FIG. 5.** Diffractograms measured at RT on an amorphous  $\text{Ge}_{0.83}\text{Sn}_{0.17}$  film deposited on the native silicon oxide formed on Si(001) and annealed at  $T = 788 \text{ K}$  for 6 min, before (top) and

after (bottom) chemical etching in a 5% HF solution (a), and SEM images obtained on the same sample before (b) and after (c) chemical etching.

**FIG. 6.** AFM measurements performed on the same sample as in Fig. 5c, after annealing at  $T = 788$  K for 6 min and chemical etching in a 5% HF solution: a) surface topography, and b) 1D topography profile along the blue line shown in a).

**FIG. 7.** X-ray diffractograms measured at RT on a 100 nm-thick Ge film deposited at RT on the Si(001) substrate and annealed at 873 K for 30 min (top) and a 100 nm-thick Ge film deposited on Si(001) at  $T = 633$  K (bottom).

**FIG. 8.** Measurements performed on the surface of a 100 nm-thick Ge film deposited at  $T = 633$  K on Si(001): a) SEM image, b) AFM image, and c) AFM profile measured along the line presented in b).

**FIG. 9.** X-ray diffractograms measured at RT on different 100 nm-thick  $\text{Ge}_{0.83}\text{Sn}_{0.17}$  films grown in different conditions on a 100 nm-thick Ge buffer grown at  $T = 633$  K on Si(001): a) deposition at the same temperature as the Ge buffer without growth interruption, b) deposition without growth interruption but stopping sample heating before  $\text{Ge}_{0.83}\text{Sn}_{0.17}$  deposition, c) deposition after stopping sample heating at the end of the Ge buffer deposition and with a growth interruption of 10 min before  $\text{Ge}_{0.83}\text{Sn}_{0.17}$  deposition, and d) crystallization of an amorphous  $\text{Ge}_{0.83}\text{Sn}_{0.17}$  film deposited at RT on the Ge buffer.

**FIG. 10.** Analyses performed on the surface of a 100 nm-thick  $\text{Ge}_{0.83}\text{Sn}_{0.17}$  film deposited on a 100 nm-thick Ge buffer grown at  $T = 633$  K on Si(001) in the conditions corresponding to Fig. 9b (no growth interruption, sample heater off): a) SEM image, b) AFM image, and c) AFM profile measured along the line presented in b).

**FIG. 11.** Chemical characterization of the 100 nm-thick  $\text{Ge}_{0.83}\text{Sn}_{0.17}$  film deposited on a 100 nm-thick Ge buffer grown at  $T = 633$  K on Si(001) in the conditions corresponding to Fig. 9b (no growth interruption, sample heater off): a) Ge and Sn atomic distributions determined by APT in the  $\text{Ge}_{1-x}\text{Sn}_x$  layer (solid symbols) compared to random distribution (solid lines) centered on 90 and 10 at%, respectively, b) part of the mass spectrum acquired by APT in the  $\text{Ge}_{1-x}\text{Sn}_x$  layer, and d) RBS measurements performed on the same sample (black) and simulations (red solid line) corresponding to the structure 100 nm-thick  $\text{Ge}_{0.0}\text{Sn}_{0.1}$ /100 nm-thick Ge /Si(001).

Khelidj et al.

Figure 1

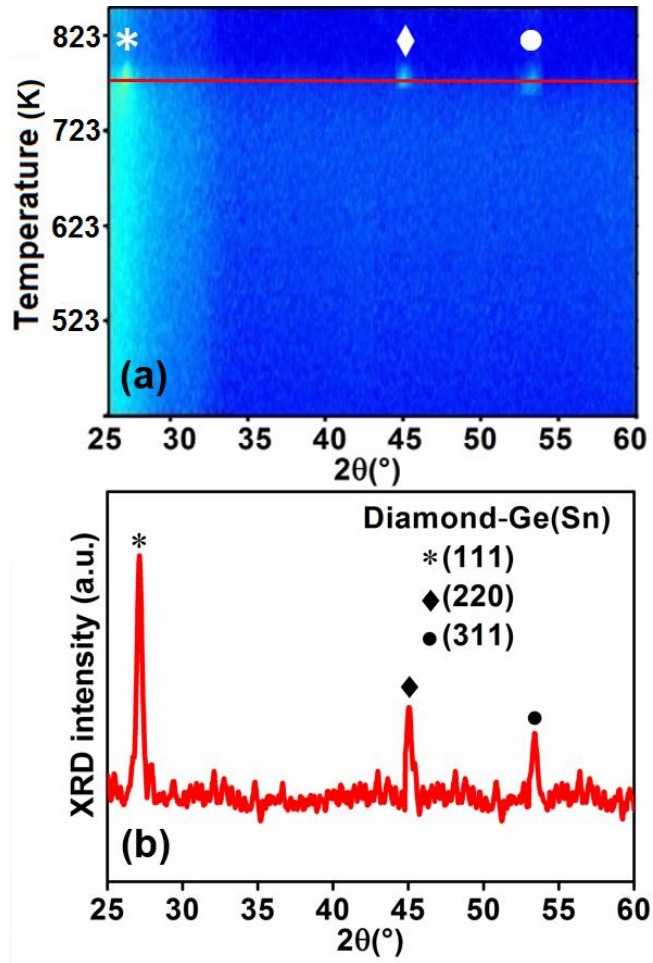


Figure 2

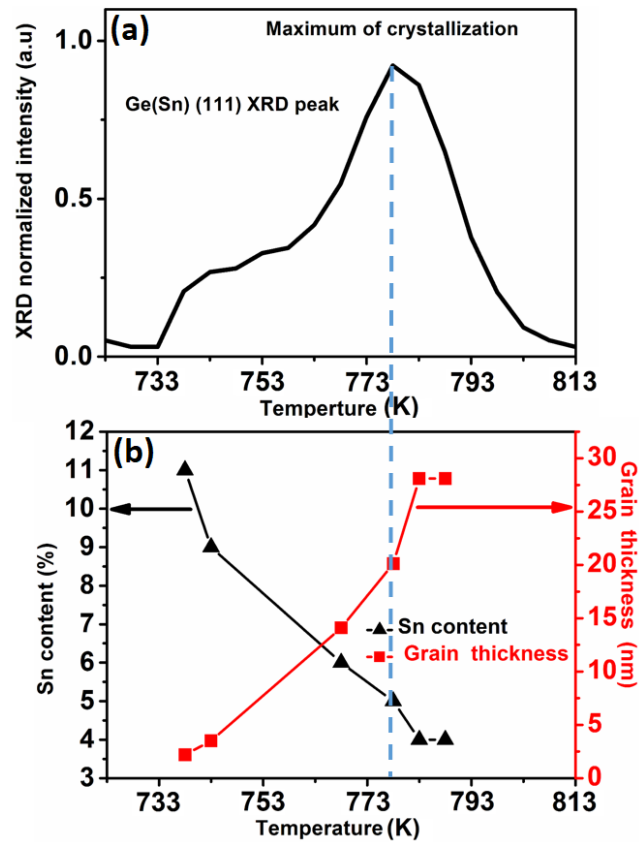
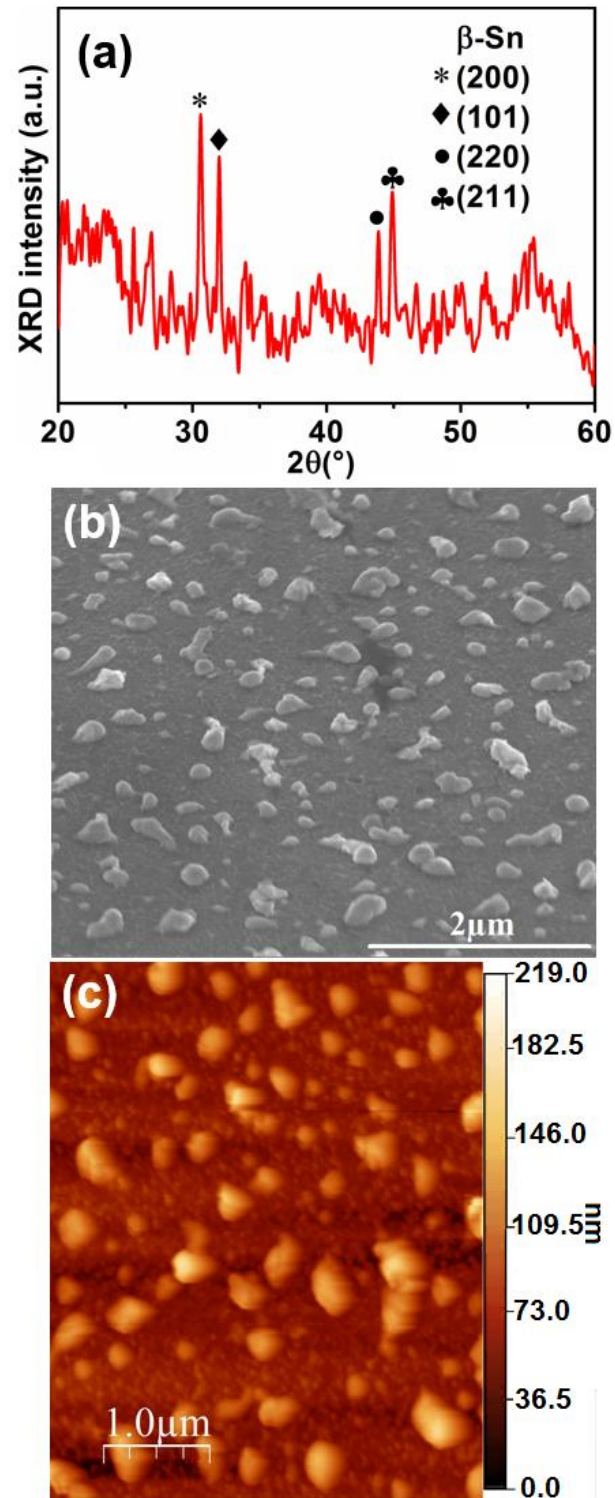


Figure 3



**Khelidj et al.**

**Figure 4**

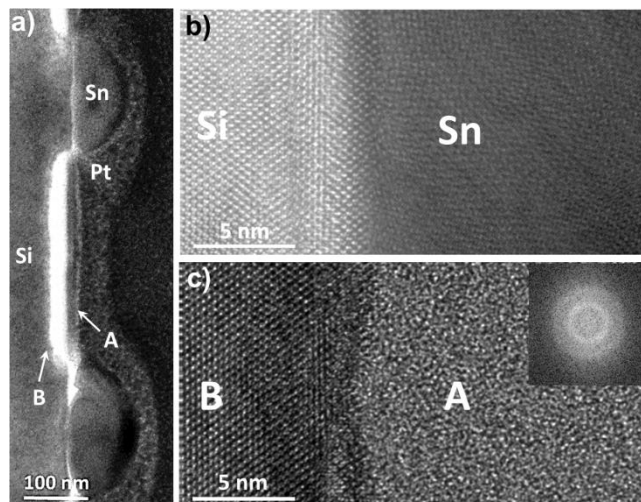


Figure 5

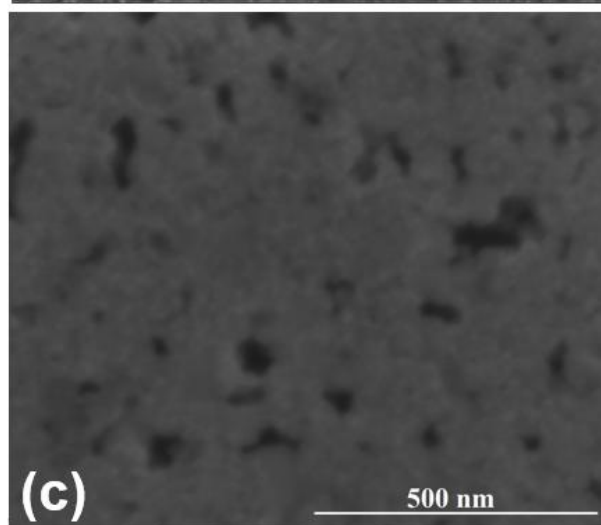
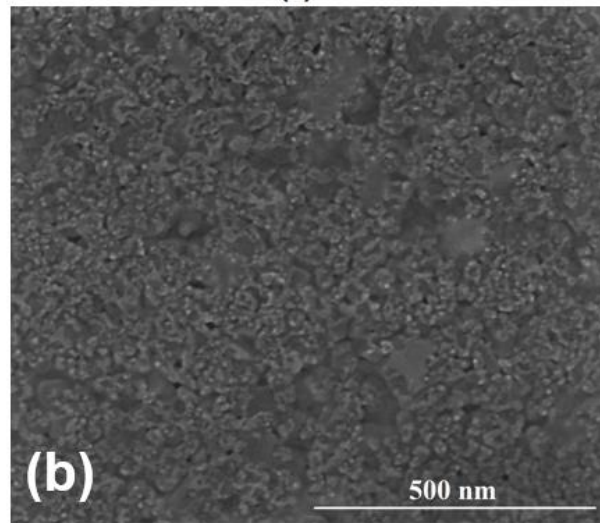
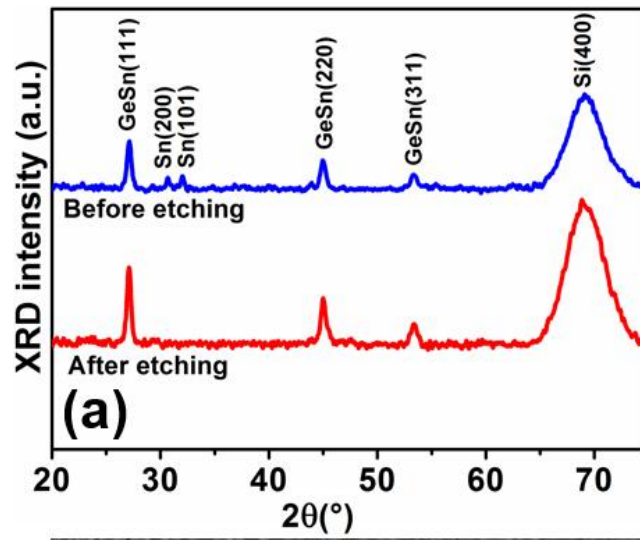


Figure 6

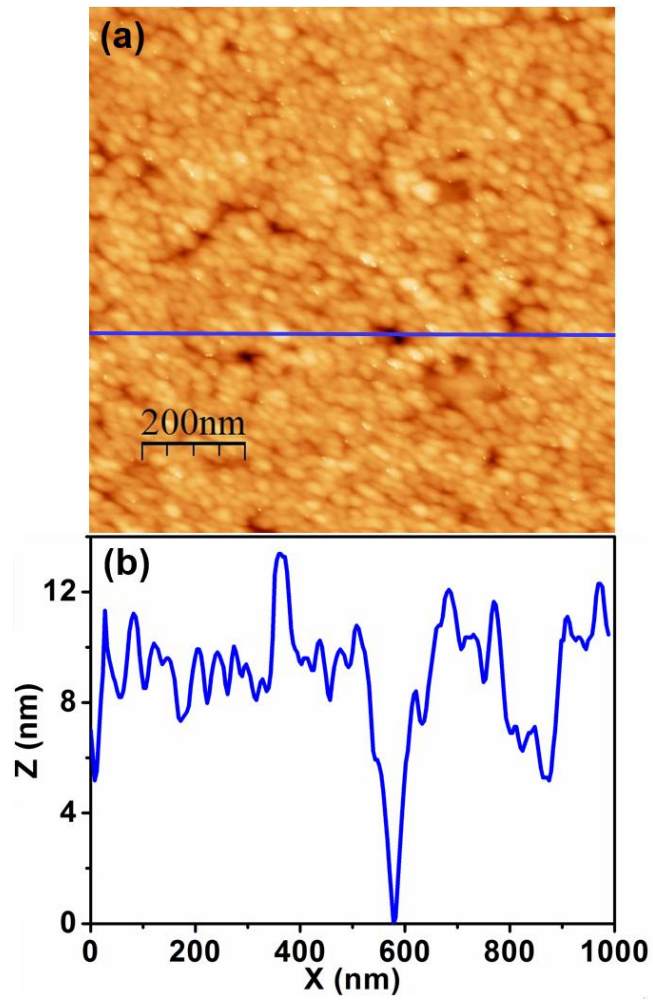


Figure 7

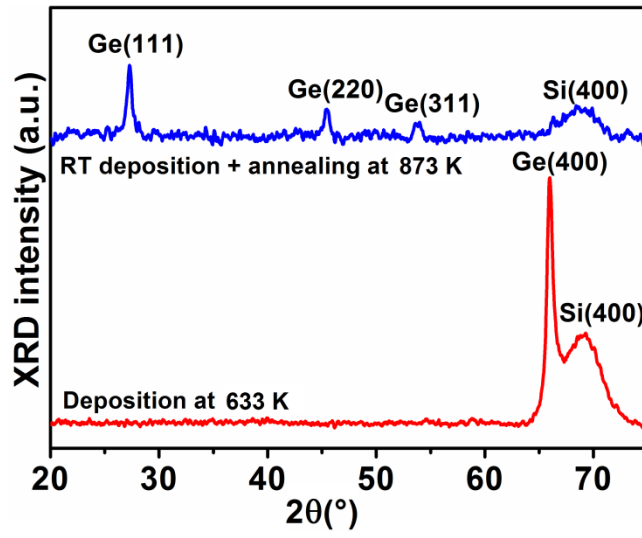


Figure 8

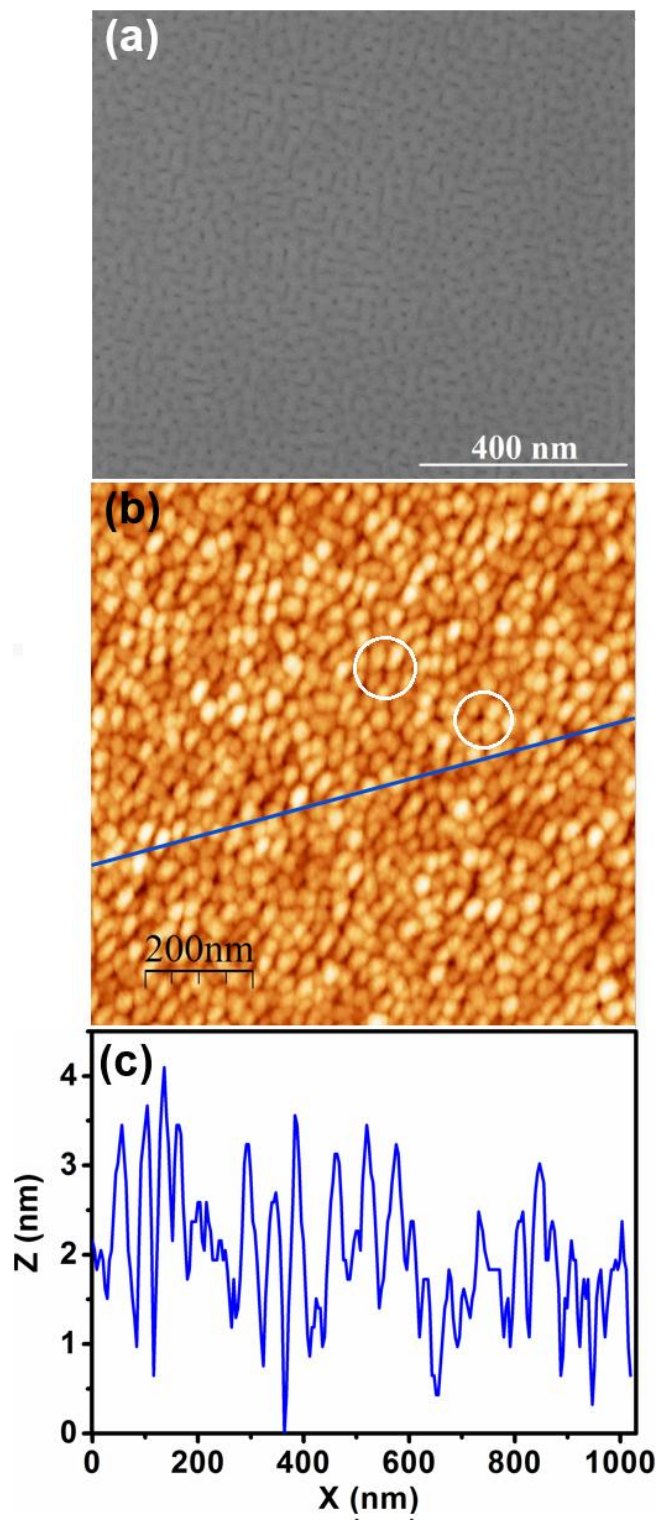


Figure 9

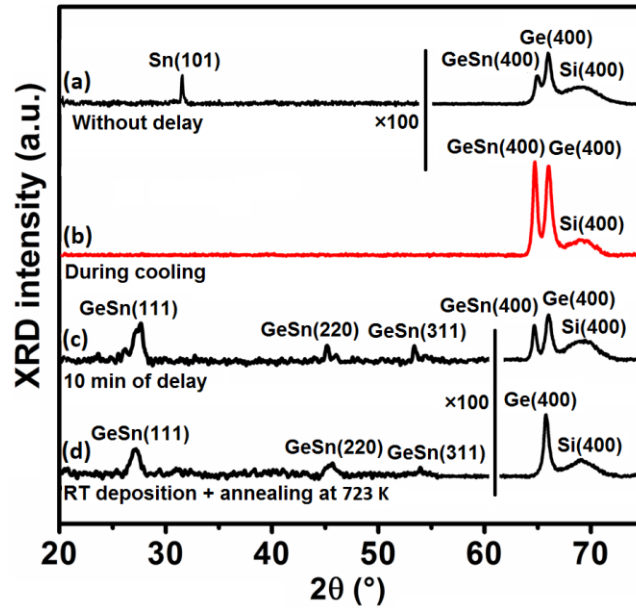


Figure 10

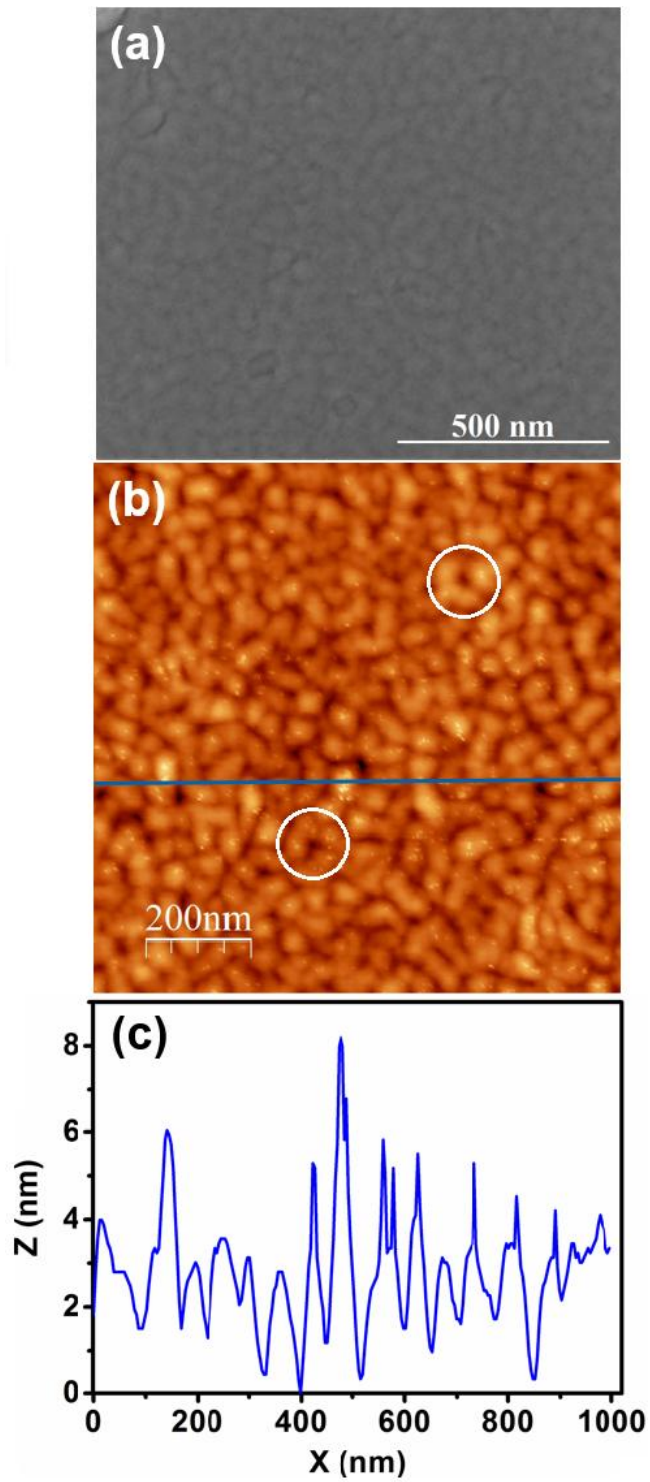


Figure 11

